

The Star Cluster Population of M51: II. Age distribution and relations among the derived parameters

N. Bastian^{1,2}, M. Gieles¹, H.J.G.L.M. Lamers^{1,3}, R.A. Scheepmaker¹, R. de Grijs⁴

¹Astronomical Institute, Utrecht University, Princetonplein 5, NL-3584 CC Utrecht, The Netherlands
e-mail: bastian@astro.uu.nl

²European Astronomical Institute, Karl-Schwarzschild-Strasse 2 D-85748 Garching b. München, Germany

³SRON Laboratory for Space Research, Sorbonnelaan 2, NL-3584 CA Utrecht, The Netherlands

⁴Department of Physics & Astronomy, University of Sheffield, Hicks Building, Hounsfield Road, Sheffield S3 7RH, UK

Received 14 April 2004 / Accepted 28 October 2004

Abstract. We use archival *Hubble Space Telescope* observations of broad-band images from the ultraviolet (F255W-filter) through the near infrared (NICMOS F160W-filter) to study the star cluster population of the interacting spiral galaxy M51. We obtain age, mass, extinction, and effective radius estimates for 1152 star clusters in a region of $\sim 7.3 \times 8.1$ kpc centered on the nucleus and extending into the outer spiral arms. In this paper we present the data set and exploit it to determine the age distribution and relationships among the fundamental parameters (i.e. age, mass, effective radius). We show the critical dependence of the age distribution on the sample selection, and confirm that using a constant mass cut-off, above which the sample is complete for the entire age range of interest, is essential. In particular, in this sample we are complete only for masses above $5 \times 10^4 M_{\odot}$ for the last 1 Gyr. Using this dataset we find: *i*) that the cluster formation rate seems to have had a large increase ~ 50 -70 Myr ago, which is coincident with the suggested *second passage* of its companion, NGC 5195, *ii*) a large number of extremely young (< 10 Myr) star clusters, which we interpret as a population of unbound clusters of which a large majority will disrupt within the next ~ 10 Myr, and *iii*) that the distribution of cluster sizes can be well approximated by a power-law with exponent, $-\eta = -2.2 \pm 0.2$, which is very similar to that of Galactic globular clusters, indicating that cluster disruption is largely independent of cluster radius. In addition, we have used this dataset to search for correlations among the derived parameters. In particular, we do not find any strong trends between the age and mass, mass and effective radius, nor between the galactocentric distance and effective radius. There is, however, a strong correlation between the age of a cluster and its extinction, with younger clusters being more heavily reddened than older clusters.

Key words. Galaxies: individual: M51 – Galaxies: star clusters

1. Introduction

This study aims at understanding the formation history of star clusters, their properties and spatial distribution in the interacting spiral galaxy M51. To study such a system, one needs the superb spatial resolution of the *Hubble Space Telescope* (*HST*) in order to avoid crowding effects and to differentiate between individual stars, associations, and compact star clusters.

Although much work has already been done on extragalactic star clusters using the *HST*, most studies have concentrated on specific components of the full cluster populations (e.g. star clusters in the center of spiral galaxies, Böker et al. 2001) or star cluster systems in extreme

environments such as galactic mergers (e.g. Miller et al. 1997, Whitmore et al. 1999). In order to form a baseline to study the effects of environment on cluster formation, evolution and general cluster properties, one must study the properties of clusters in normal (i.e. more common) environments. It is only then that we are able to see which properties are truly unique for a given environment and which properties remain fixed across all environments.

One such property of star cluster systems that has a well-established baseline is that of the luminosity function. Larsen (2002) has shown that the cluster populations of spiral galaxies follow a luminosity distribution that is well represented by a power-law, $N(L) \propto L^{-\alpha}$, with $\alpha=2.0$. This is remarkably similar to that found in all other environments (de Grijs et al. 2003c), and hence can be re-

garded as a general property of young star cluster systems. Recent work by Larsen (2004) shows that young clusters in spiral galaxies have typical sizes of $R_{\text{eff}} \sim 3\text{-}10$ pc, with the youngest clusters having extended halos. It remains to be seen how other properties, such as mass, age and spatial distributions depend on the environment in which the clusters form.

M51 provides an almost ideal astrophysical laboratory to study extragalactic star clusters. This is due to its relatively close distance of ~ 8.4 Mpc (Feldmeier et al. 1997) and its almost face-on orientation. Physically it is an interesting case study because it seems to have had a strong interaction with its companion, NGC 5195 an S0 peculiar galaxy, during the last few hundred Myr, which presumably caused its grand design spiral appearance as well as its high star formation rate. The M51/NGC 5195 encounter(s) have been modelled in great detail by many authors; this will allow us to compare the derived age distribution of the star clusters with the orbital parameters of the system, which are robustly established. The system has been modelled relatively successfully by a single early passage $\sim 300 \pm 100$ Myr ago (Toomre & Toomre 1972, Hernquist 1990, and Salo & Laurikainen 2000, hereafter SL00). Additionally, SL00 propose a model of a double passage, the first happening $\sim 400\text{-}500$ Myr ago and the second, or last encounter, happening $\sim 50\text{-}100$ Myr ago. This latter model seems to fit many observed details that the single passage models fail to reproduce, such as the observed counter-rotation of the southern HI tail.

Much work has already been done on the star cluster system of M51. A full literature review is beyond the scope of this paper, but we refer the reader to the following work: Bik et al. (2003, hereafter Paper I) have studied the star cluster population in a relatively small area to the north east of the nucleus that included inner sections of one of the spiral arms. They find that the mass function is reasonably well fit by a power-law of the form $N(M) \propto M^{-\alpha}$ where $\alpha \sim 2.0$. They also show that there is weak evidence for a possible increase in the cluster formation rate in the inner spiral arms at ~ 400 Myr ago, the proposed time of an interaction between M51 and NGC 5195, but that the evidence is only at the 2σ level. Boutloukos & Lamers (2003) used the data from Paper I to determine the characteristic disruption timescale of clusters in this region, which is ~ 40 Myr for a $10^4 M_{\odot}$ cluster. Larsen (2000) has studied a few of the “young massive clusters” which form the high end of the luminosity function, using combined *HST* and ground-based observations. He finds that although M51 has a relatively high star-formation rate, it fits the specific *U*-band luminosity (T_L^U) vs. star formation rate relation of non-starburst galaxies. This has been interpreted as showing that high-mass star clusters will form whenever the star formation rate is high enough. Scoville et al. (2001) have used many of the same *HST* images used in this study, to look at OB star formation in M51. They find that the mass function of OB star clusters is well represented by a power law of the form $N(M_{\text{cl}})/dM_{\text{cl}} \propto M_{\text{cl}}^{-2.01}$, in agreement with the results

presented in Paper I. They also show that although the spiral arms only make up $\sim 25\%$ of the disk surface area they contain a much higher fraction of the catalogued HII regions.

This study is the second in a series of three, which aim at understanding the properties of the star cluster system of M51 as a whole. This paper introduces the data and techniques used to determine the cluster properties, analyses the age distribution as well as the correlations among the cluster parameters, namely their age, mass, extinction, size, galactocentric distance, and position in the galaxy. In the third paper (Gieles et al. 2004, hereafter Paper III) we determine the luminosity and mass distributions and derive the disruption timescale for clusters in M51.

The study is setup in the following way: in § 2 we present the observations used in this study, including the reduction and photometry. In § 3 the methods of finding the clusters and the selections applied to the data are elucidated. In § 4 we present our method of determining the ages, extinctions, and masses of each of the detected clusters, and discuss how contaminating sources are detected and removed. In §§ 5 and 6 the general properties of the cluster system are presented and discussed, while § 7 presents evidence for a young, short lived cluster population. In §§ 8 and 9 the size distribution and relations between size and the other cluster parameters are presented, followed by § 10 in which we summarize our main results.

2. Observations, reduction and photometry

Our analysis of stellar clusters in M51 is based on observations done with the *Wide Field Planetary Camera-2* (WFPC2) and the *Near-Infrared Camera and Multi-Object Spectrometer* (NICMOS) on board the *HST*.

2.1. WFPC2 Observations

Observations in 8 different passbands of the inner region of M51 were obtained from the *HST* data archive: F255W (\approx UV), F336W (\approx U), F439W (\approx B), F502N (\approx OIII), F555W (\approx V), F656N (\approx H α), F675W (\approx R) and F814W (\approx I). We emphasize that we have not transformed the *HST* filters into the standard Cousins-Johnson filter system.

An overview of the filters and exposure times is given in Table 1. Proposal ID 5777 and 7375 contain the F555W band images and will be referred to as Orientation 1 and Orientation 2, respectively. All the other orientations are rotated/shifted to these 2 base orientations. An overview of the orientation of the data sets is shown in Figures 1 and 2. The combined data sets span a region of about $180'' \times 200''$ (i.e. 7.3×8.1 kpc) containing the complete inner spiral arms of the galaxy.

The raw images were flat fielded using the automatic standard pipeline reduction at the Space Telescope Science Institute (STScI). Warm pixels were removed us-

ing the `warpix` task which is part of the IRAF/STSDAS¹ package. Bad pixels were fixed with the `wfixup` task which interpolates over bad pixels in the x -direction.

Cosmic rays were treated differently for the three datasets. For the images consisting of multiple exposures of the same field per filter the task `crrej` was used. This combines exposures of the same field by rejecting very high counts on an individual pixel basis. Three iterations were done with rejection levels set to 8, 6 and 4σ .

In single exposure images the cosmic rays were removed using the `Lacos_im` package of van Dokkum (2001). This algorithm identifies cosmic rays of arbitrary shapes and sizes by the sharpness of their edges and reliably discriminates between poorly sampled point sources and cosmic rays. The parameter setting used was a `sigclip` of 6.5, a `sigfrac` of 0.5 and an `objlim` of 4. Four iterations were done to give the best result, because the result of the cosmic ray rejection is very sensitive to the settings. Careful tests were done to make sure no real sources were removed by the cosmic ray removal task. This resulted in almost cosmic ray free images. The few remaining cosmic rays will be rejected later when the photometry coordinates from the source detection in the different filters will be cross correlated.

2.2. NICMOS Observations

NICMOS images were obtained with the NIC3 camera, which has a field of view (FoV) of about $52'' \times 52''$. A mosaic of nine overlapping pointings of the NIC3 camera of M51 was available in the archive, yielding a total FoV of $186'' \times 188''$ (i.e. 7.6×7.7 kpc) of the central region in the near-infrared F110W and F160W filters (see Fig. 2). Each of the nine mosaic positions was observed using a square dither in each filter setting.

Flat-fielding, dark frame correction and bias subtraction were all performed in the pipeline image reduction and calibration by the `calnica` task. Bad pixels were repaired with the `fixpix` task which uses static bad pixel mask images. All individual images in the dither pattern were shifted to the same orientation with `imshift`. The dither pattern constituted of shifts of an integer number of pixels, the images were perfectly aligned on subpixel level. The individual images in the same orientation were added with `imcombine` using the `crrej` method for cosmic ray rejection. Finally, the nine co-added images were mosaiced by matching sources in the overlap region and comparing histograms of the sky values. This results in a large square FoV overlapping a large area of the optical data set. Since the mosaic routine does not scale the count rates values

when matching the individual chips, the mosaic images can be used for source selection and photometry.

2.3. Source selection

Point-like sources were identified in the individual WFPC2 chip images and the NIC3 mosaic images with the `daofind` task from the DAOPHOT package Stetson (1987). For the optical filters a threshold of 5σ was used, where σ is the sky noise. In order not to be biased towards certain areas on the chips, the value of σ was determined on a low background region on each of the chips. For the F255W filter the threshold was 4σ and for the near-infrared NIC3 images the threshold was set to 8σ . The threshold was chosen such that in each filter and chip the resulting source density was more or less the same. No limitation was set on sharpness or roundness, to include as many sources as possible, including unrelaxed young clusters.

2.4. Photometry

2.4.1. WFPC2

The coordinates from the source lists, obtained from the `daofind` output, were used as an initial guess of the centers for the `phot` aperture photometry routine. For the WF chips we used an aperture, annulus (inner boundary of background annulus) and dannulus (width of the background annulus) of 3, 7 and 3 pixels respectively. For the PC chip we used slightly larger values, namely 4, 10, 3 for the aperture, annulus and dannulus respectively. The cho-

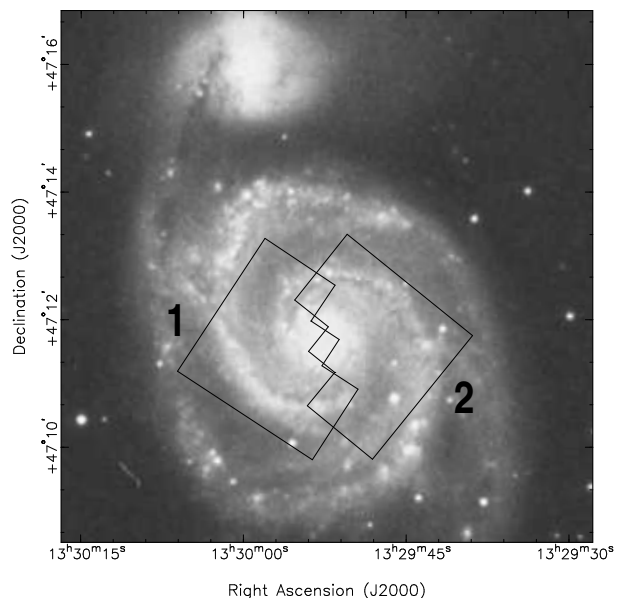


Fig. 1. The orientation of the two *HST* pointings for the F336W, F439W, F555W, F675W, F814W, and F656N filters overlaid on a *Digital Sky Survey* image of M51. North is up, and east is to the left. The left orientation/pointing is referred to as field 1, while the right is referred to as field 2.

¹ The Image Reduction and Analysis Package (IRAF) is distributed by the National Optical Astronomy Observatories, which is operated by the Association of Universities for Research in Astronomy, Inc., under cooperative agreement with the National Science Foundation. STSDAS, the Space Telescope Science Data Analysis System, contains tasks complementary to the existing IRAF tasks. In this study Version 2.1.1 (December 1999) was used.

Table 1. Overview of the datasets used.†Equivalent to the V3 Position Angle of the WFPC2.

ID	Filters	Exp. time	Observation Date	Orientation angle†
7375 (WFPC2)	F336W	2 x 600 s.	21 July 1999	275.9
	F439W	500 + 600 s.		
	F555W	2 x 600 s.		
	F656N	1300 + 700 s.		
	F675W	500 s.		
	F814W	700 + 300 s.		
5777 (WFPC2)	F439W	2 x 700 s.	15 Jan 1995	101.5
	F555W	600 s.		
	F675W	600 s.		
	F814W	600 s.		
5123 (WFPC2)	F502N	400 + 1400 s.	24 January 1995	93.2
	F656N	500 + 1200 s.		
5652 (WFPC2)	F255W	4 x 500 s.	12 May 1994	333.0
	F336W	2 x 400 s.		
7237 (NICMOS3)	F110W	128 s.	28 June 1998	-113.2
	F160W	128 s.		

sen values for the apertures are ~ 3 times larger than the FWHM of the PSF in order to account for the fact that at the distance of M51, clusters appear slightly extended (i.e. are not point sources). Photometric calibration was done by applying zero-point offsets from Table 28.2 of Voit (1997) in the VEGAMAG system.

Total magnitudes were determined by correcting for flux outside the measurement aperture. Ideally aperture corrections are determined from real sources on the image. In the case of our data there were not enough isolated bright sources located in regions of low background to obtain a meaningful correction. Thus aperture corrections from the measurement aperture radius to a $0.5''$ radius were determined from analytically generated clusters by convolving a PSF (generated using *Tiny Tim*, Krist & Hook 1997) with King profiles using the *Baolab* package (Larsen 1999). King profiles of concentration factor, c , of 30 ($c = r_t/r_c$ where r_t is the tidal radius and r_c is the core radius), and effective radius, R_{eff} , of 3 pc (see § 8) were used for the analytic cluster profiles. The values for the three WF chips are averages. For the PC and WF chip in each filter the values are listed in Table 3. A final -0.1 mag. correction was applied to all sources to correct for the light missed in the $0.5''$ aperture. After applying the aperture corrections, the magnitudes were corrected for CTE loss according to the equations of Whitmore et al. (1999a).

2.4.2. NICMOS

The photometry procedure for the NIC3 images is essentially the same as for the WFPC2 images. An aperture, annulus and dannulus of 2, 5 and 3 pixels were used, respectively. The flux was converted to magnitudes in the VEGAMAG system using the PHOTFNU values from the headers. Aperture corrections from the measurement aperture radius to a $1.0''$ radius were determined using

the same technique as for the WFPC2 images. Values are listed in Table 2. A final correction to a nominal infinite aperture correction of -0.08 mag (i.e., multiplying the flux with 1.075) was applied.

2.5. Incompleteness due to detection limits

In order to quantify at what magnitude our sample starts to be incomplete due to detection limitations, the 90% completeness limit was determined for each band for each pointing. To this end, artificial sources were added to the *HST* images and were recovered with exactly the same routines as used to find the real sources. A very important criterion is that objects should be 5 times above the standard deviation of the background. The value for σ should be the same as when real sources are found. The magnitude of the added sources were determined and an error criterion of $\Delta\text{mag} < 0.2$ was applied (see § 3), the same criterion as for the real sources to enter the photometry list. The tests were done for the PC1 and WF3 chips of both pointings separately.

Extended sources with different R_{eff} are simulated by convolving WFPC2 PSFs, produced by *Tiny Tim*, with King profiles. The King profiles are produced by the *Baolab* package (Larsen 1999). King profiles with a concentration index, c , of 30 with different R_{eff} were tried. In § 8 it is shown that the average size for *resolved* clusters in M51 is ~ 3 pc. Thus, we take a more conservative estimate of the completeness survey by assuming $R_{\text{eff}} = 5$ pc (the more extended the cluster is the more diffuse it becomes, for a given brightness, making it more difficult to detect). On each chip, two regions were studied, one with low and one with high background levels. Since the aperture corrections were derived for average extended sources ($R_{\text{eff}} = 3$ pc), the magnitudes of the artificial 5 pc sources are too faint and the magnitudes of the pure PSFs are too bright. In both cases the maximum offset is about 0.15 mag.

The recovered fraction as a function of magnitude in the F555W filter is plotted in Fig. 3 for the WF3 chip. Each plot shows the effects of background and source size. The plots show that for an individual chip the 90% completeness limit varies by more than a magnitude, depending on the location on the chip and the size of the source. We therefore do not have a clear detection limit but a region where incompleteness sets in. Details of this effect and its influence on the luminosity function are given in Paper III. The worst case 90% completeness limits are shown in Fig. 4 for all bands and for the 3 available *HST* pointings. When more than one pointing is available for a filter, the brightest (i.e. most conservative) 90% completeness limit of that filter is chosen.

For the remainder of this study the worst case 90% completeness limit was applied to the data. Since the PC chip has been shown to have many single bright stars (Lamers et al. 2002) and since its completeness limit is about 1 magnitude brighter than for the WF3 chip, we will only use the WF data for the remainder of this study.

3. The selection of the clusters and the photometry master list.

The coordinate lists for the individual WFPC2 chips were transformed to one system using the `metric` task. This task corrects for geometric distortion and yields coordinates with respect to one frame (WF3). Transformation matrices to convert the mosaic coordinates of field id #5652 (F255W and F336W) (see Table 1) to Orientation 1 and Orientation 2 coordinates, were determined by finding sources in common to both frames in the F336W filter. Since the #5777 program does not contain an F336W exposure, the F439W exposure was used instead. The sources used to find the transformations were selected to

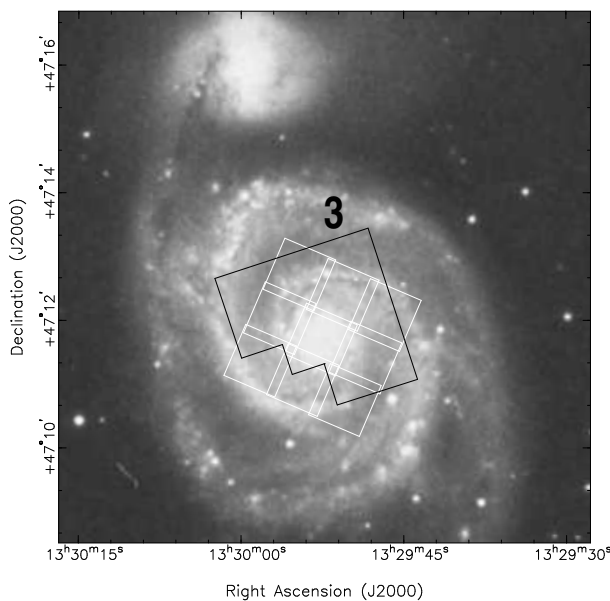


Fig. 2. The orientation of the F255W FoV (black) and the NIC3 mosaic (white).

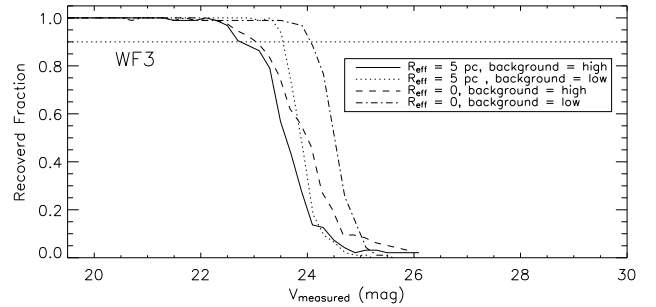


Fig. 3. Recovered fraction of sources added to the F555W science images on the WF3 chip. Four examples are shown, combinations of low and high background and PSFs and extended clusters ($R_{\text{eff}} = 5$ pc).

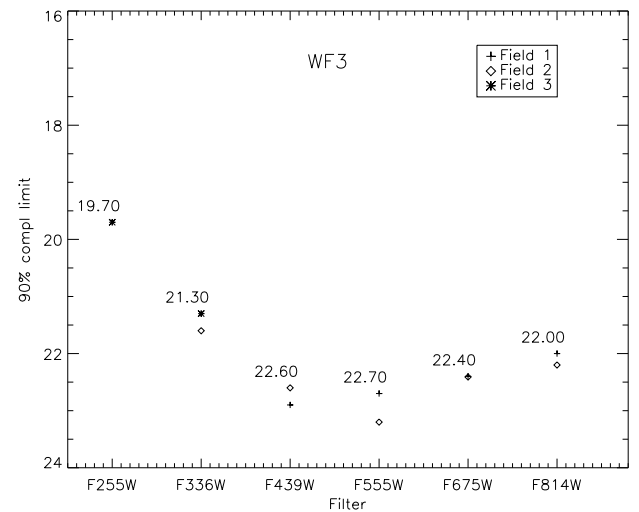


Fig. 4. Worst case (high background, $R_{\text{eff}} = 5$ pc clusters) 90% completeness limits for PC1 and WF3 for all filters and the three available *HST* pointings.

be isolated and spread over the images by as much as possible to make the transformation as accurate as possible. The spatial transformation functions were calculated based on the coordinates of the sources in the two frames using the `geomap` task in IRAF. The accuracy of the transformation is approximately 0.1-0.2 pixels. The same was done for the near-infrared filters (F110W and F160W). For these transformations identical sources were found in the F110W and F814W bands. In this case the accuracy was somewhat lower since the NIC3 pixel size ($\approx 0.2''$) is larger than the WF pixel size ($\approx 0.1''$). The accuracy of the transformation function is still 0.2-0.3 WF pixels.

The final source list was made by cross correlating sources found in the various filters. First, a cross correlation between the F439W, F555W and F675W was done. If a coordinate was found in all 3 filters, allowing a mismatch of 1.4 pixels, it was defined as a genuine source.

Table 2. 90% completeness limits for the WF3 in the 3 different available pointings. Most conservative values are printed bold.

Filter	PC1			WF3		
	1	2	3	1	2	3
F255W	-	-	18.80	-	-	19.70
F336W	-	20.8	20.45	-	21.60	21.30
F439W	22.10	21.80	-	22.90	22.60	-
F555W	21.80	21.90	-	22.70	23.20	-
F675W	21.20	21.90	-	22.40	22.45	-
F814W	21.20	21.00	-	22.20	22.20	-

Table 3. Aperture correction values for all filters (mag).

Filter	PC	WF3 (mean)	NIC3
F225W	-0.32	-0.14	
F336W	-0.31	-0.13	
F439W	-0.31	-0.13	
F555W	-0.32	-0.13	
F675W	-0.32	-0.13	
F814W	-0.33	-0.14	
F110W			-0.22 ± 0.01
F160W			-0.22 ± 0.01

[†] This value is applied to our sample. For clusters with $R_{\text{eff}} = 5$ pc, these values decrease by ~ 0.15 mag. (e.g. to -0.28 for F555W in the WF3 chip).

Then the other filters were compared with the source list, again allowing a mismatch of 1.4 pixels. The transformed coordinates of the F255W and F336W frame were allowed to have a 1.6 pixel mismatch. The F110W and F160W frames were allowed to have a 1.8 pixel mismatch. This was adopted because of the uncertainty in the transformation.

The resulting initial source list contains 3504 objects that are observed in at least the F439W, F555W, and F675W bands above the 5σ detection limit. Most of these will be eliminated later in the study of their energy distributions because the photometry is uncertain or the energy distribution does not match that of cluster models (see § 4.5).

3.1. Contamination of the sample by stars

We estimate the possible number of massive stars that may contaminate our source sample by scaling the star population of the LMC, measured by Massey (2002) to the conditions in M51. This sample, which is complete down to $V \simeq 15.7$ mag or $M_V \simeq -3.2$ mag covers a total area of 10.9 kpc^2 and includes most of the bar, the 30 Doradus region and several other well populated fields. This area contains more than half of the mass of the LMC. We have calculated the intrinsic visual magnitudes, by

adopting only foreground extinction of $A_V = 0.40$ mag and $E(B - V) = 0.13$ mag (Massey et al. 1995) and a distance modulus of 18.48 mag (Westerlund 1997) The total number of stars brighter than $M_V < -7.0$ mag (which corresponds to $V < 22.60$ at the distance of M51, for no extinction) is less than 100, and the number with $M_V < -8.0$ mag is 6. By far the majority of these stars are found in clusters. We can get an estimate of the fraction of the luminous *field* stars compared to the total fraction from the data in Table 12 of Massey (2002) which gives the number of massive stars outside clusters. (This is the only large and homogeneous extragalactic stellar sample deep enough to determine the relation between the populations of field stars and the total populations.) He found 186 field stars (i.e. outside known OB associations) more massive than $40 M_\odot$, which corresponds to $M_{\text{bol}} \leq -9$ mag. More than 90 per cent of these are on or near the main sequence, where $T_{\text{eff}} > 25\,000$ K and hence the bolometric correction is so large that $M_V > -7.0$ mag. At most 10% of these stars, i.e. less than 18, are optically bright at $M_V < -7.0$ mag in the LMC.

With a total mass of the observed area of about $4 \times 10^9 M_\odot$ (Meatheringham 1991), this implies about 4 to 5 field stars more massive than $40 M_\odot$ per $10^9 M_\odot$. (This number could be slightly higher if the dark matter content of the LMC within the region used here is considerable). This small number is due to the very steep IMF of the massive field stars. Massey (2002) showed that the stellar IMF of massive field stars can be approximated with $\Gamma \simeq -4$, compared to $\Gamma \simeq -1.3$ for cluster stars, where $\Gamma = 1 + d(\log N(M))/d(\log(M))$.

The total luminous mass of M51 within a radius of 5 kpc is $2.1 \times 10^{10} M_\odot$ (Salo & Laurikainen 2000). Scaling the number of field stars per unit mass in the LMC to that of M51, we estimate that at most 170 to 210 field stars with $M_V < -7.0$ will be in our field, and less than 15 to 20 with $M_V < -8.0$, *if there were no extinction in M51*. Even a moderate extinction will remove these stars from our sample.

Another estimate of contaminating stellar sources in our sample can be obtained by comparing the number of field stars to that of observed clusters. This comparison relies on the assumption that the ratio of field stars to clusters is the same in different galaxies. This assumption will not be valid for low or intermediate mass stars between galaxies with widely different cluster disruption timescales, as galaxies with shorter disruption timescales will have a higher field star to cluster ratio. However, for young massive stars (lifetimes less than 10 Myr), disruption is not expected to significantly influence this ratio. Using the catalog of Bica et al. (1996) we see that there are ~ 180 clusters and associations brighter than $M_V = -6.94$ in the LMC (assuming a distance modulus to the LMC of 18.48 and an imposed completeness of $m_V = 22.70$ at the distance of M51). Using the arguments given above, there are < 18 young massive stars that are brighter than $M_V = -7.0$ in the LMC. Thus there are less than one field star for every ten clusters in the LMC. Therefore, using

this approximation, we expect less than 10% of our M51 sample to be bright young stars.

A third alternative method to estimate the contamination by massive isolated field stars is to scale the number of isolated field stars in the LMC to that of M51 using the mass normalized star formation rates. In the studies summarized by Grimm et al. (2003), M51 has about half the star formation rate per unit galaxy mass as the LMC. So, using this assumption we expect half as many bright field stars in M51 as in the LMC per unit mass, which results (using the mass ratios above) in ~ 47 bright field stars.

We conclude that the number of contaminating stars in our sample is small². Moreover, we will show in Section 4.5 that most of these will be removed from the sample because they do not pass the criterion that their energy distribution can be fitted with a cluster model.

4. Determination of the cluster parameters from their energy distribution

The age, mass and extinction of star clusters can be derived by comparing their spectral energy distributions to those of cluster evolution models (e.g. Paper I, de Grijs et al. 2003a,b,c). This method can also be used to eliminate contaminating sources (e.g. stars and background galaxies).

4.1. Adopted cluster models

We have adopted the updated GALEV simple stellar population (SSP) models (Schulz et al. 2002, Anders & Fritze v. Alvensleben 2003) as our templates to derive ages, extinction values, and masses for each of the observed clusters in M51. These models use the isochrones from the Padova group, which seem to fit the data better than the Geneva tracks (Whitmore & Zhang 2002). The set of models that we use assumes a Salpeter stellar IMF from 0.15 - 50 M_{\odot} . We have used models with metallicities of 0.4, 1, and 2.5 Z_{\odot} , and a comparison between the different metallicities will be made in Section 4.6.

There were two major reasons for selecting the updated GALEV tracks. The first is the inclusion of gaseous emission lines as well as continuum emission, which can severely affect the broad-band colours for young star clusters (see Anders & Fritze-v. Alvensleben 2003). The second is that they have been published in the *HST* WFPC2/NICMOS filter system, which eliminates possible inaccuracies in converting the *HST* observations to the standard Cousins-Johnson system.

² Bik et al. (2003) found that massive young clusters in the inner NE-spiral arm of M51 have a surprisingly small flux in the O[III] $\lambda 5007$ line. They interpret this as evidence that there is a lack of massive stars of $M > 30M_{\odot}$ in the clusters. If this is also valid for the field stars, the number of contaminating field stars in our sample will be even smaller than estimated here.

4.2. The fitting of the spectral energy distributions

We used the three-dimensional maximum likelihood fitting method (*3DEF*) developed by Bik et al. (2003). The method has been described in detail there, and hence we will only give a brief summary of it here. In passing we note that this method has been tested against colour-colour methods of age fitting, and has shown itself to be superior (e.g., de Grijs et al. 2003a vs. Parmentier, de Grijs & Gilmore 2003).

The method works as follows: we use a grid of SSP models, i.e. the GALEV models (see previous section) that give the broad-band colours of a single age stellar population as a function of age. For each model age, we apply 50 different extinctions in steps of 0.02 in $E(B - V)$. We adopted the Galactic extinction law of Savage and Mathis (1979), which was found to agree with the extinction law derived for M51 by Lamers et al. (2002). We then compare the model grid with the observed spectral energy distribution of the clusters using a minimum χ^2 test, with each observation weighted with its uncertainty. The model (age and extinction) with the lowest χ^2 is selected, and the range (i.e. maximum and minimum age) of accepted values is calculated by taking the most extreme model that satisfies $\chi_{\nu}^2 < \chi_{\nu, \min}^2 + 1$. Once the age and extinction have been calculated, the mass is found by comparing each observed filter magnitude to each model magnitude (iteratively with respect to age and extinction). Since we have first scaled the GALEV models to a *present mass* of $10^6 M_{\odot}$ the difference between the observed and the predicted magnitude (taking into account the distance modulus and extinction) can be converted to the present mass of the observed cluster³.

4.3. Test of the accuracy of the method

We have tested the accuracy of the method used for the determination of the age and mass of clusters. To this purpose we created a grid of synthetic clusters, distributed evenly in logarithmic age, in the range of $7.0 < \log(t/\text{yr}) < 10.0$ in 31 steps, and evenly in logarithmic mass in the range of $3.0 < \log(M/M_{\odot}) < 6.0$ in 21 steps. This results in 651 synthetic clusters. The clusters have a distance modulus of $m - M = 29.64$, as for M51, and were assigned a random extinction of $0 < E(B - V) < 1.0$ mag with a Gaussian probability function that peaks at $E(B - V) = 0$ mag and has a $\sigma = 0.20$ mag. For each of these clusters we calculated the expected energy distribution in the same *HST*/WFPC2 filters as used for this study of M51, using the GALEV cluster models with a metallicity of $Z = 0.02$, and a Salpeter IMF. The photometry of each synthetic cluster was given an uncertainty

³ All masses derived in this paper refer to the *present mass* of the clusters, not to their *initial mass*. If stellar evolution is the only mass loss mechanism of the cluster, the initial mass of the clusters can be retrieved by correcting the present mass for the fraction lost by stellar evolution, given by the GALEV models.

Table 4. Empirical parameters for the uncertainty of the magnitudes: $\Delta(m) = 10^{d_1+d_2 \times m}$

Filter	d_1	d_2
F255W	-8.540	+0.390
F336W	-7.850	+0.325
F439W	-8.320	+0.328
F555W	-7.800	+0.300
F675W	-7.600	+0.300
F814W	-8.230	+0.328

that depends on magnitude. The uncertainty was derived from the observations, which show that $\Delta(m)$ can be approximated quite well by $\Delta(m) = 10^{d_1+d_2 \times m}$, where m is the magnitude and the values of d_1 and d_2 are empirically determined for each *HST* filter. These values are listed in Table 4. We then added a random correction to the magnitude of each cluster in each filter, within the interval $(-\Delta(m), +\Delta(m))$. This resulted in a list of 651 synthetic clusters with photometry and photometric errors similar to those of the observed clusters in M51.

We then ran these synthetic clusters through our cluster fitting program to determine the age, mass and extinction in exactly the same way as done for the observed clusters. We adopted the same conservative magnitude limits as for the observed sample, as given in Table 2. The comparison between the input mass, age and extinction of the synthetic clusters and the result of the fitting gives an indication of the accuracy and reliability of the results. The result is shown in Figure 5.

The panels show the difference between input and output values of $\log(t)$, $\log(M)$ and $E(B-V)$ as a function of the V magnitude of the synthetic cluster. This parameter was adopted because the accuracy of the fitting is expected to depend on the accuracy of the input photometry, for which V is a good indicator. We have divided the results into four age bins (with parameters indicated in the figure), because the accuracy of the fit may be different in different age intervals, as the spectral energy distribution depends on age.

Figure 5a shows that the age determination is quite accurate, to within about 0.20 dex, for relatively bright clusters with $V < 21.0$ mag. For fainter clusters with $V > 21.0$ mag the uncertainty increases up to a maximum of about 1 dex for clusters with $V > 22.0$ mag. The scatter is approximately symmetric around the zero-line with two exceptions.

- (i) For the youngest faint clusters with $t < 30$ Myr and $V > 21.5$ mag the age is more likely to be overestimated than underestimated. This is the consequence of the simple fact that the two youngest GALEV cluster models have ages of 4 and 8 Myr. So a cluster cannot be fitted to a model younger than 4 Myr, which limits the possible negative values of $\log(t_{\text{out}}/t_{\text{in}})$.
- (ii) Faint clusters with ages of $\log(t/\text{yr}) > 7.5$ have a

higher probability to be fitted with a younger cluster model than with an older cluster model. This might reduce the number of old clusters derived from the fitting of the SEDs of observed clusters. This effect will be taken into account in the analysis of the observed mass and age distributions of the M51 clusters.

Figure 5b shows that the mass determination is quite accurate for relatively bright clusters with $V < 21.0$ mag. For fainter clusters with $V > 21.0$ mag the uncertainty decreases up to a maximum of about -0.5 dex to $+1.0$ dex for the faintest clusters. The scatter is approximately symmetric around the zero-line, except for the tendency to overestimate the mass of the faint old clusters. This is a direct result of the underestimate of the age.

Figure 5c shows that the extinction can be derived quite accurately for young clusters with $\log(t/\text{yr}) < 8.5$ and $V < 21.5$ mag. For fainter clusters there is a symmetric scatter up to about $\Delta E(B-V) \simeq 0.1$ mag. For clusters older than 300 Myr there is a tendency to overestimate the extinction. This is the reason for the overestimate of the mass and the underestimate of the ages of these old clusters.

In general the ages and masses derived from fitting the cluster models are quite accurate: more than 99% of our synthetic clusters have an age determination that is accurate to within 0.25 dex and a mass determination that is accurate to within 0.2 dex. For real cluster samples the accuracy will depend on the magnitude distribution of the clusters, and hence on their photometric accuracy.

4.3.1. Stochastic colour fluctuations

An additional uncertainty in the fitting of ages of star clusters using SSP models, is the stochastic colour fluctuations resulting from the fact that young low mass clusters will be dominated by a few high luminosity stars (e.g. Dolphin & Kennicutt 2002). Thus, the absence (or presence) of a small number of stars can significantly affect the observed integrated colours of a cluster. Unfortunately, due to the random nature of this effect it is impossible to determine which clusters in our sample are most heavily affected by this. However, if the stochastic colour fluctuations vary equally around the 'true' (i.e. fully sampled, high mass limit) colour, we do not expect our derived age distribution for the population as a whole to be affected by this. Finally, we note that our age distribution analysis (see § 6) has been restricted to clusters with derived masses above $10^{4.7} M_{\odot}$, e.g. the most massive clusters, where the stochastic colour fluctuations are expected to be smallest (Lançon & Mouhcine 2000). Stochastic effects are expected to affect the colour and magnitude of a 10 Myr, $10^5 M_{\odot}$ cluster by $\sigma_V = 0.08$ mag and $\sigma_{V-I} = 0.07$ (Dolphin & Kennicutt 2002). These small fluctuations are within the observational uncertainties, and as such are not expected to significantly affect the derived parameters.

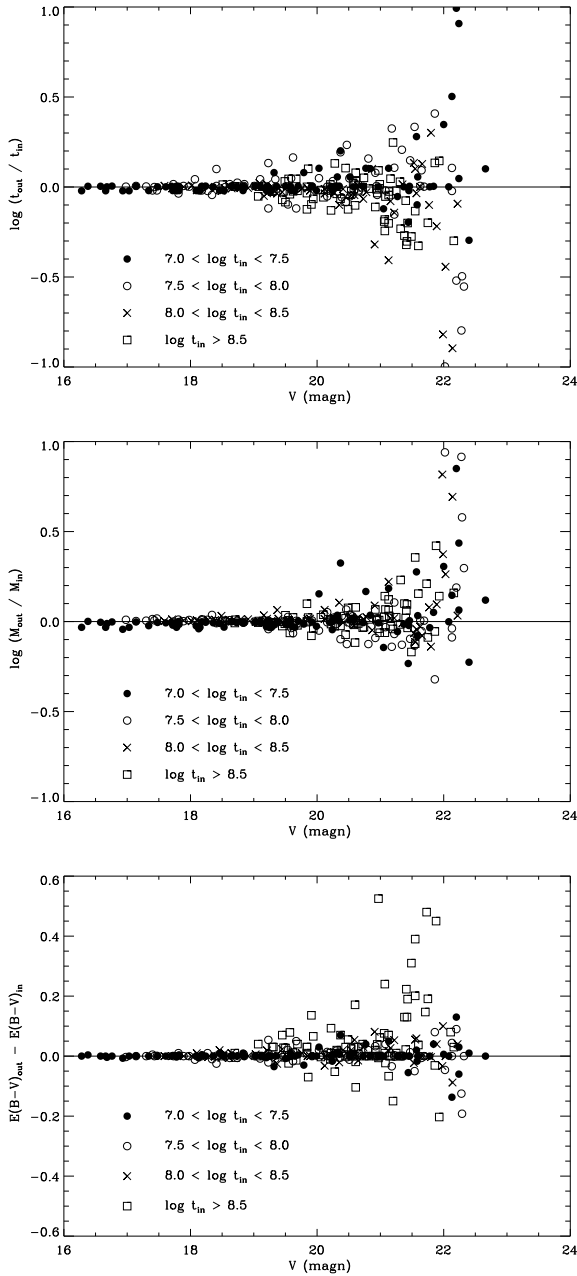


Fig. 5. Comparison between input and output values of the ages (upper panel, a), masses (middle panel, b) and extinction values (lower panel, c) of the synthetic cluster sample. Different symbols indicate different age ranges.

4.3.2. Dependence on the adopted models

The *3DEF* method assumes that the adopted models accurately reproduce the colours of star clusters as a function of age. In order to quantify this effect we have carried out the same analysis as discussed in § 4.3, but now using the Starburst99 models (Leitherer et al. 1999) for the artificial clusters, and then carrying out our fitting procedure using the GALEV models. These models were chosen because of the differing stellar evolutionary isochrones used when

constructing their respective SSPs (i.e. the GALEV models adopt the Padova isochrones, while the Starburst99 models adopt the Geneva isochrones).

These tests resulted in 80% of the artificial clusters being fit within 0.5 dex of the input age and mass. The extinction is fit to within 0.2 mag in $E(B-V)$ for $> 80\%$ of the artificial clusters. Thus we see that while there are significant differences between the models used, the parameters of the majority of clusters can be accurately recovered.

We also note that fitting our cluster sample using the Starburst99 models as templates, resulted in age and mass distributions which are consistent with the results presented here (Bastian & Lamers 2003). Namely, the high numbers of very young (< 10 Myr) as well as the increase the cluster formation rate at $\sim 50 - 100$ Myr ago (see § 6).

4.4. Reduction of the sample based on energy distributions

Once we have obtained the best fit for each source (i.e. age, extinction and mass) we can then determine whether or not the object has a *good* fit, i.e. if it is a cluster. In previous studies (Paper I, de Grijs et al. 2003a) we used the selection criterion that the reduced χ^2 must be below 3.0. This was effective in eliminating most of the poor fits, but it also removed many of the brightest clusters because their photometric error was relatively low. In order to remove this problem, we have used the standard deviation, defined to be

$$\sigma^2(BVR) = \sum_i \frac{(m_i^{\text{mod}} - m_i^{\text{obs}})^2}{n_{\text{filters}}} \quad (1)$$

where the sum runs over the F439W, F555W, and F675W bands only (the three bands in which all clusters were detected), as a criterion to test the accuracy of the photometric fit. The sum was restricted in order to maintain a fairly homogeneous set and to eliminate biases that would occur if bands with short exposures or low count rates (e.g. F255W) were included.

We then checked by eye the spectral energy distributions of the sources and their fits, in order to find a reasonable value for the minimum $\sigma^2(BVR)$, $\sigma_{\text{min}}^2(BVR)$. As the “goodness” of the fit is rather arbitrary, we quantified the exact value of $\sigma_{\text{min}}^2(BVR)$ by making a histogram of all the sources, approximating the histogram with a Gaussian (which is a relatively good fit) and taking the $1/e$ point. This point, and the value preferred by our visual inspection were almost identical at $\sigma_{\text{min}}^2(BVR) = 0.05$.

In the remainder of the paper, when we refer to “clusters”, we will mean sources that passed the following criteria:

- detected in the F439W, F555W, and F675W bands at at least 5σ above the background,
- photometric uncertainty < 0.2 mag in the F439W, F555W, and F675W bands,
- detected in at least one other band,

- well fit ($\sigma^2(BVR) < 0.05$) by an SSP model,
- brighter than the 90% completeness limits for each filter in which they are detected (see Table 2)

1150 clusters pass these criteria, which will be used to study the cluster population in M51. The majority of the sources (from the original 3504 sources detected) that have been removed from our sample were eliminated because they were fainter than one or more of our 90% completeness limits.

4.5. The elimination of stars on the basis of their energy distribution

In § 3.1 we argued that the expected number of very luminous stars that might contaminate our sample is relatively small. We have investigated the rejection of possible stellar sources from our sample on the basis of the energy distribution fitting. To this purpose we created energy distributions of stellar atmosphere models and analysed them in the same way in which we analysed the energy distributions of clusters.

We adopt the supergiant models calculated by Bessell et al. (1998), transformed to WFPC2 magnitudes by Romaniello et al. (2002). Bessell et al. (1998) normalized the magnitudes to stars with a radius of $1 R_{\odot}$ at a distance of 10 pc. They published 70 models with T_{eff} ranging from 3500 to 50000 K for a range of gravities from main sequence stars to supergiants. We adopted the energy distributions of these stellar models with the lowest gravity (without adding noise to their photometry) and then analysed the data as if the stars were clusters. We did this for stars that are observed in all six *WFPC2* bands (UV,U,B,V,R,I), and for stars observed only in the U,B,V,R bands or in the B,V,R,I bands.

We found that stars with effective temperatures higher than about 14,000 K all end up in the youngest age bin for clusters of $\log(t/yr) \simeq 6.6$. If our sample is contaminated by massive stars, most of these will be blue, because they spend most of their time on or near the main sequence. If there is a red phase for such massive stars, the crossing time between the blue and the red phase is very short, only about 1% of the main-sequence phase. However stars with masses in excess of $50 M_{\odot}$ are not expected to become red supergiants because that would bring them above the observed Humphreys-Davidson luminosity upper limit (Humphreys & Davidson, 1979). We conclude that, *if* there is a sizable number of massive O-stars with $21.70 < V < 22.70$ mag, they will end up in the youngest age bin of our cluster sample.

Fig. 6 shows the values of $\sigma^2(BVR)$ as a function of the temperature of the stars, for stars observed in all six *WFPC2* bands, and for stars observed only in the B,V,R,I or U,B,V,R bands. Only stars below the dashed line pass our criterion of $\sigma^2(BVR) < 0.05$. We see that most of the stars will be rejected from our sample, except the coolest ones.

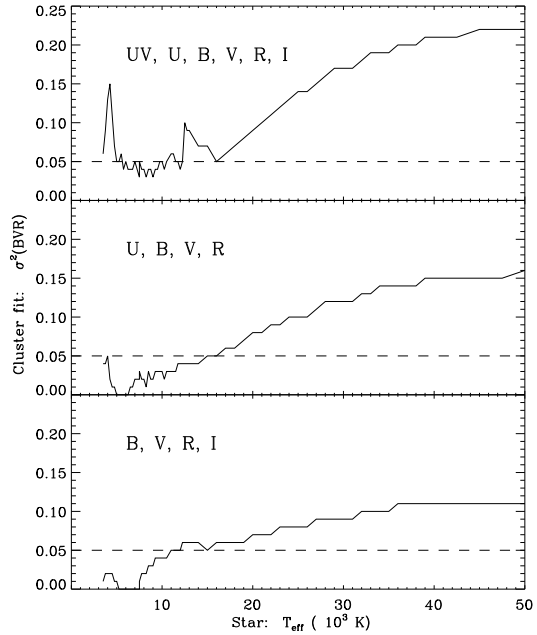


Fig. 6. The elimination of possibly contaminating bright stars in our sample by means of the fitting of their energy distribution. The figure shows the values of the rejection criterion $\sigma^2(BVR)$ (Eq. 1) for stars of different temperatures in three different filter combinations. Notice that possibly contaminating stars with $T_{\text{eff}} > 17\,000$ K will be effectively eliminated by our selection criterion $\sigma^2(BVR) < 0.05$.

We concluded before (Sect. 3.1) that the expected contamination of our cluster sample of sources with $V < 21.70$ mag with bright stars is very small. Here we have shown that our analysis of their energy distribution will eliminate a major fraction of these. The small number that may pass our selection criterion, are expected to end up in the youngest age bin.

4.6. The effect of metallicity

We have studied the effect of metallicity on the determination of the age, mass, and extinction of the clusters. To this purpose we follow the method of de Grijs et al. (2003a,b) and introduce metallicity into our models as a free parameter.

This technique has been applied recently to NGC 3310 (de Grijs et al. 2003b) with good results, and to NGC 6745 (de Grijs et al. 2003c) with somewhat less encouraging results as two metallicities were equally well represented in the final sample, due to the smaller number and narrower wavelength coverage of available passbands, and the inherent effects of the age–metallicity degeneracy. For NGC 3310 the authors report that the near-infrared colours of a cluster are a good indicator of metallicity, while optical colours do a better job at discerning ages (see also Anders et al. 2004).

To this end we have fit all sources in M51 which pass our criteria (see § 4.4) with models of four metallicities, namely $Z = 0.004, 0.008, 0.02,$ and 0.05 . We do not find any significant difference in the number of sources that pass our selection criteria ($\sigma^2(BVR) < 0.05$) between the different metallicity models. We find that 14%, 21%, 17%, and 48% of the sources in our sample are best fit (lowest $\sigma(BVR)^2$) by models of $Z = 0.004, 0.008, 0.02,$ and 0.05 respectively. The largest percentage of the clusters being fit by twice solar metallicity models is consistent with the metallicity estimates of HII regions in M51 by Hill et al. (1997).

We note however, that many of the individual clusters within the same cluster associations show widely different metallicities. As this seems unphysical, we are forced to conclude that fitting on metallicity is not possible with the current data. We therefore choose to concentrate our analysis on the fits using the solar metallicity models (which is the median metallicity found in our sample), although we will discuss how our results depend on the assumed metallicity where applicable.

4.7. Recovery rates

In order to determine the recovery rate of the fitting method we use the artificial cluster sample generated in § 4.3. In Fig. 5 we found that the accuracy of the fit depended on the magnitude of the input cluster, with brighter clusters being fit with higher accuracy. Because of the input cluster IMF, which has many more fainter clusters than brighter ones, we need to quantify this affect. The recovery rate is defined to be the number of clusters found divided by the number of input clusters for a given age bin. Figure 7 shows the recovery rate as a function of age. This shows that we slightly over-predict the number of clusters in the age range of $\log(t/\text{yr}) \in [6.62, 6.87]$ and $\log(t/\text{yr}) \in [7.37, 7.62]$ by about 40 per cent. We underestimate the number of clusters in the age range of $\log(t/\text{yr}) \in [6.87, 7.12]$ by about 20%, and also tend to underestimate the number of clusters with ages greater than 10^8 yr. This is not a physical effect but due to the rapidly changing colours of the SSP GALEV models during this age range. We will use this recovery rate in § 6.2 where we study the cluster formation history of M51.

5. Extinction

Once we have derived ages, extinctions, and masses for all of the clusters, we can begin looking at general trends in the cluster population.

Figure 8 shows the distribution of the $E(B - V)$ values for different age groups. The left-hand side of the figure shows the number of clusters and the right-hand side shows their logarithmic values. The figure shows that at each age bin over half of the detected clusters have an extinction of $E(B - V) < 0.05$ mag, with the rest showing a rapidly declining distribution up to $E(B - V) \simeq 0.8$ mag. The logarithmic figures show about the same distri-

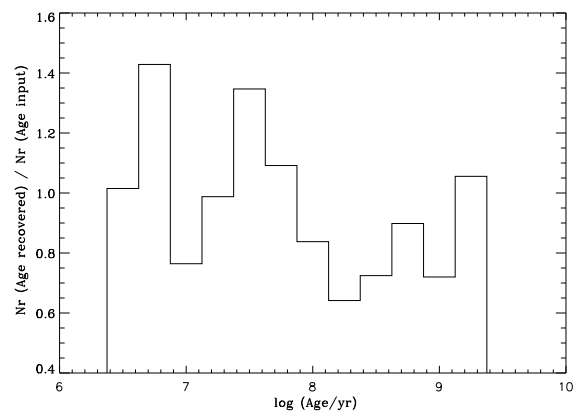


Fig. 7. The recovery rate of our sample as a function of input age. We underestimate the number of clusters in the range of $6.9 < \log(t/\text{yr}) < 7.1$ by about 25% and overestimate the number in the preceding age bin by $\sim 40\%$.

bution of the clusters with $E(B - V) > 0.05$ mag, with $d \log(N)/dE(B - V) \simeq -2.0$. This relation is independent of age, although the highest extinction found decreases strongly with ages. This is presumably due to the fading of clusters as they age, bringing them closer to the detection limit, so older clusters with a significant amount of extinction will drop below the detection limit. Another effect that could contribute to the observed distribution is if young clusters have more extinction than older clusters, which is expected as young clusters form in gas rich environments.

The large numbers of clusters found with low extinction is qualitatively what is expected. The cluster IMF of $N(M) \sim M^{-\alpha}$, with $\alpha \simeq 2$, implies an increase in cluster numbers towards the lower mass and fainter clusters. The magnitudes of these low mass clusters are close to the detection limit, so they can only be detected if their extinction is small. Thus our sample is complete to larger extinction values for brighter clusters, and for younger ages which are less affected by the detection limit (see Fig. 10). This effect will affect all cluster studies where the host galaxy is not optically thin (i.e. studies where one cannot see through the host galaxy at the given completeness limits).

In Fig. 9 we show the extinction as a function of age for the clusters in our sample. The solid points are the mean of all the points for each age bin and the error bars represent the variance about the mean. This figure shows that the average extinction is higher for young clusters (≤ 20 Myr) and rather abruptly drops to a constant value for clusters older than 20 Myr. This is qualitatively what is expected as clusters emerge from their parent molecular cloud, although as we noted above, there is a selection effect which causes us to detect younger clusters to higher extinction values.

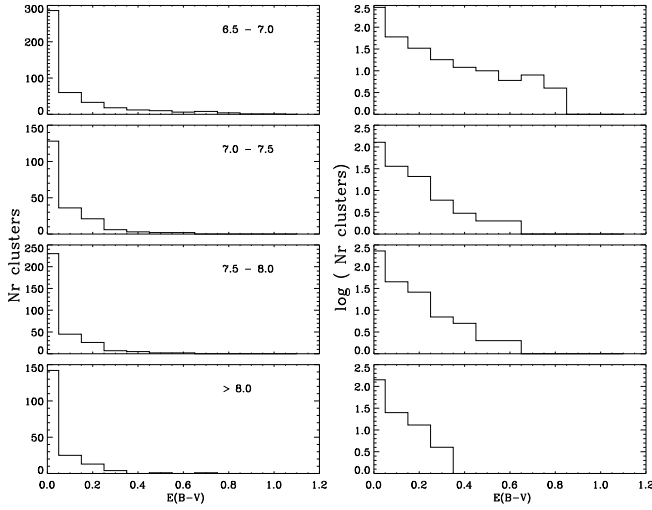


Fig. 8. The histograms of the extinction for different age bins (given in the upper right of the panels in the left column, in logarithmic years). The left-hand panels show the linear distribution (N versus $E(B-V)$) and the right-hand panels show the logarithmic distribution ($\log(N)$ versus $E(B-V)$). Notice the strong peak near $E(B-V) \simeq 0$ mag and the steeply declining relation towards $E(B-V) \simeq 0.8$ mag.

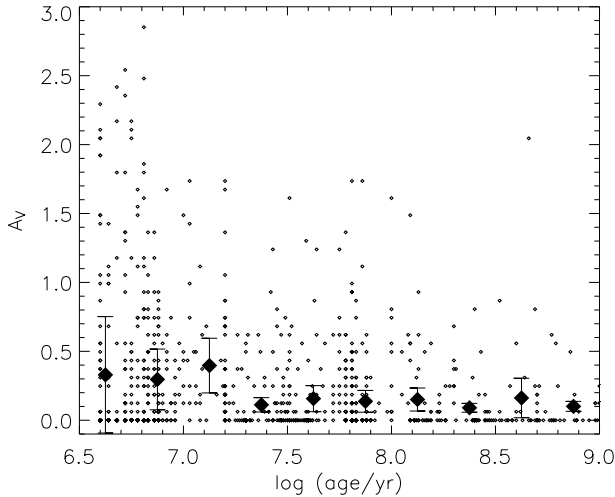


Fig. 9. The extinction as a function of age for the clusters in our sample. The solid points are the mean for each age bin, while the error bars are the variance about the mean. Note that the extinction is higher for clusters with ages less than 20 Myr than for the older clusters.

6. The age distribution of the clusters

It has been shown that the global properties of the host galaxy, such as an interaction or merger, can significantly affect the cluster formation rate (CFR) within a galaxy

(e.g. de Grijs et al. 2003a). To search for such an effect within M51, we combined our cluster sample, with the detailed models of the interaction between M51 and its companion, NGC 5195, taken from the literature (SL00). SL00 propose a scenario in which NGC 5195 has had two close passages with M51, an early encounter at approximately 400-500 and a second at 50-100 Myr ago (the last passage). Their *double encounter* model reproduces the kinematic features of the system better than the single passage models (such as, e.g., the apparent counter-rotation of the southern HI-tail), as well as the morphological “kink” in the northern spiral arm.

6.1. The mass versus age diagram

Figure 10, top panel, shows the age of each cluster plotted against its determined mass. (We remind the reader that this is the present mass of the cluster.) Note the presence of a clear lower mass limit which increases with age. This is due to the evolutionary fading of clusters as they age, which raises the minimum mass that the clusters should have to be brighter than our detection limit. Hence, the lack of old low-mass clusters is mainly an effect of fading due to stellar evolution (another important effect is cluster disruption, which will be treated in Paper III). The solid lines increasing to the right show the detection limit for $m_{F555W} = 22.7$ mag, i.e. the adopted magnitude limit of the sample, and 21.7 mag.

The figure shows the apparent concentrations of the clusters in some very narrow age bins, i.e. at $\log(t/yr) = 7.2, 7.3$ and near 7.8. This is not a physical effect but it is due to the way we select the best fitting models in the study of the cluster SEDs with the 3DEF-method (see § 4.3 and Paper I). In reality these peaks should spread over the neighbouring age bins.

The bottom panel in Fig. 10 shows the relation between the age and masses of those clusters whose sizes are resolved. The general properties are the same as for the full sample, namely the increase in the lower mass limit as a function of increasing age, an excess of clusters with young ages (< 10 Myr), and an additional excess at 60 Myr. Therefore we conclude that we are not biasing our study by including unresolved sources.

As mentioned above, certain artifacts of the age vs. mass distribution are likely caused by model and fitting effects, which do not reflect anything physical. Since this complicates the analysis, we attempt to correct for these effects using the simulations from § 4.7. To do this, we generate a number density grid in the age vs. mass space for our observed cluster sample as well as for our simulated cluster sample (cluster IMF with slope -2.0 , continuous cluster formation rate, and random extinction between $0 < E(B-V) < 1$ mag with a Gaussian probability function that has $\sigma = 0.20$ mag). The model number density is normalized in order that the average is the same as the observations (i.e. we normalize to the cluster formation rate). We then divide the observed cluster distribution by

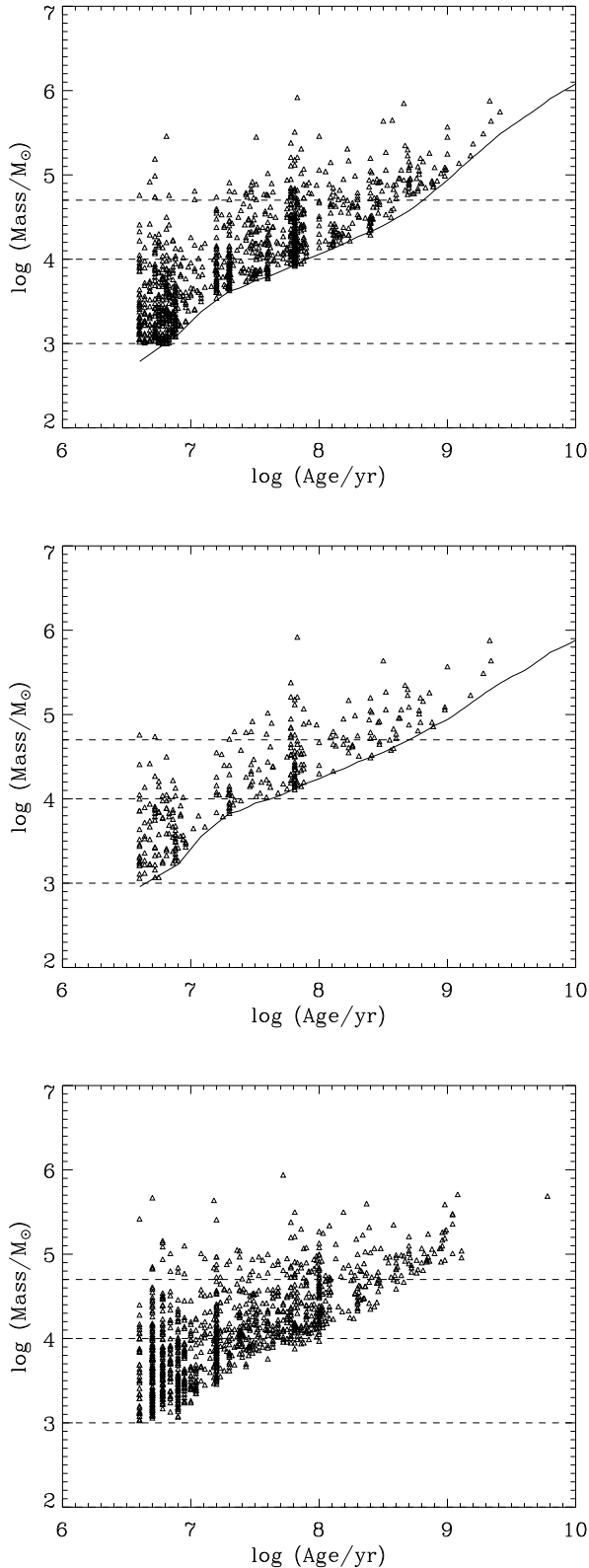


Fig. 10. Top: The present mass as a function of age for the 1078 clusters that pass our σ criterion and which have a present mass greater than $1000 M_{\odot}$. The solid line is the predicted detection limits using the GALEV models, for $m(\text{F439W}) = 22.6$ mag. The horizontal dashed lines represent constant mass cutoffs used in Fig. 12. **Middle:** The same as above, but only for those clusters with measured sizes greater than 2 pc. The solid line is the predicted detection limit for $m(\text{F555W}) = 22.0$ mag. **Bottom:** The present mass as a function of age while leaving metallicity

that of the simulated distribution. This technique will remove any features caused by the adopted models or the fitting method.

This process and the result are shown in Fig. 11. It shows the number density of the clusters in the mass versus age diagram in a logarithmic grey-scale, normalized in such a way that the number densities run from light to dark grey. The top panel shows the density of the *observed* clusters in the mass versus age diagram. The middle panel shows the density of the *generated* cluster sample with a constant cluster formation rate and a power law cluster IMF. The lower panel shows the *ratio* of the observed to predicted cluster number densities in the diagram. For the top and middle panels, dark shading represent high numbers of clusters, while for the bottom dark shading represents an over-density of observed clusters compared to that expected from the models. In order to fully interpret the final result, it is important to understand the simulated cluster sample. Two of the strongest features in Fig. 11b are the increase in the number density from the top of the panel to the bottom as well as from left to right. The increase in the number of clusters at lower masses (top to bottom in Fig. 11b) is due to the cluster initial mass function, which gives many more low-mass than high-mass clusters. The increase in the number (for a given mass bin) of clusters from younger to older (left to right) is due to the logarithmic age-binning and the assumed constant cluster formation rate in linear time.

Once we divide our observed distribution (Fig. 11a) by the simulated distribution (Fig. 11b) we have the *true* age vs mass distribution which is shown in Fig. 11c. Since the effects of the cluster IMF and the logarithmic binning have been removed in this comparison, the decrease in number density from the lower left of Fig. 11c to the upper right is presumably caused by the disruption of the clusters. Additionally we find relative excesses in the number density at ages of ~ 60 Myr and ~ 6 Myr. These two features will be discussed in more detail in § 6.2 and § 7, respectively.

6.2. The cluster formation history

In the previous section we found an excess of clusters at ages ~ 60 Myr, corresponding in time to the *last* passage of NGC 5195 and M51 in the SL00 models. In order to quantify this excess we will look at the age distribution directly (i.e. by collapsing the mass axis in Fig. 11c). As shown in § 6.1, for a given magnitude-limited sample, we are able to detect clusters to lower masses for younger ages than for older ages. Therefore, we will detect more younger than older clusters (assuming the standard cluster IMF which predicts many more lower mass than higher mass clusters), simply due to selection effects. Thus, in order to trace the true age distribution of the sample, the analysis must be restricted to masses above a certain limit, where the sample is complete for the age range of interest. This effect is shown in Fig. 12 by looking at the age distribution

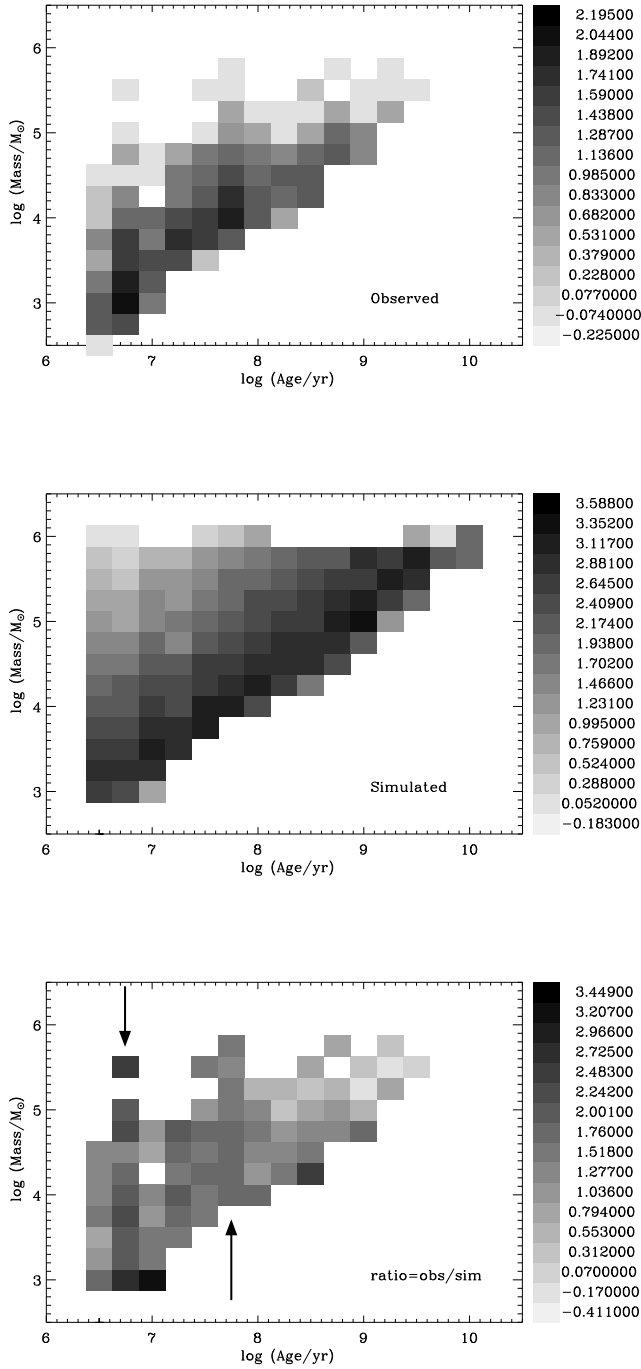


Fig. 11. **Top(a):** The present mass as a function of age for the 1152 clusters that pass our selection criterion. The shading represents the logarithmic number density, with the scale given on the right. **Middle(b):** Same as (a), but for the simulated cluster sample with a constant cluster formation rate (see § 4.3 for details). **Bottom(c):** The ratio between the observed distribution (top) and the predicted distribution (middle). The arrows indicate two age bins which have an overdensity of clusters relative to the simulated cluster sample.

and applying the constant mass cuts shown in Fig. 10. The mass cuts are at 10^3 , 10^4 , and $5 \times 10^4 M_\odot$, the last one chosen so that we are complete for ages younger than 1 Gyr.

The left-hand side of Fig. 12 shows the number of clusters detected per logarithmic age bin while the CFR (in number per Myr) is shown on the right-hand side. For the calculation of the CFR, we have corrected the age distribution of the detected clusters for the recovery rates (Fig. 7) in order to eliminate spurious effects. The difference in appearance between the two sides is due to the logarithmic binning of the left-hand side (e.g. each bin spans a larger age range than the preceding bin). Note that the distributions for different mass cuts appear very different.

If we look at the sample in which we are complete for the past Gyr (i.e. for masses $> 10^{4.7} M_\odot$) we see a clear indication of an increase in the CFR ~ 60 Myr ago. In addition, we also find the peak at ~ 6 Myr, that was seen in Fig. 11c. This peak is presumably due to the presence of a large number of unbound clusters, and will be discussed in detail in § 7.

The increase in the CFR at ~ 60 Myr ago for clusters with $\log(M/M_\odot) > 4.7$ occurs at the time of the proposed second encounter between M51 and NGC 5195. The CFR appears to have been 2 to 3 times higher during the burst period than in the period immediately preceding it. The CFR declines slightly after the initial rise, but remains significantly higher than before. In Fig. 12 we note the CFR rises extremely rapidly at the onset of the burst, and decays much more smoothly, consistent with a linear Gaussian distribution plotted on a logarithmic scale.

6.2.1. Duration of the burst

An increase in the CFR at the time of an interaction has been shown for other galaxies, e.g. M82, NGC 3310 and NGC 6745 (de Grijs et al. 2003a,b,c, respectively). While the duration of the burst of cluster formation in M51 is rather short lived, we note that this is similar to the distribution observed in NGC 3310 (de Grijs et al. 2003b) where the estimated duration of the increase in cluster formation rate was ~ 20 Myr (it should be noted that their method of analysis was very similar to the one presented here). Presumably, the increase in the CFR in M51 was likely caused by the tidal interaction between M51 and NGC 5195 ~ 60 Myr ago, supporting the *two encounter* model of SL00.

Tidal interactions can influence large portions of a galaxy within a relatively short time, and is the only known mechanism that could coordinate galaxy-wide starbursts on the timescales presented here. Recently, Murray et al.(2004) have shown that there is an Eddington-like maximum luminosity for starburst galaxies. This luminosity is a critical luminosity where there exists a balance between gravity and radiative pressure caused by the young stars formed. When a starburst is tidally triggered, as is the case in M51, the (starburst) luminosity can

grow rapidly. When this growth happens on a shorter time scale than the dynamical (free fall) timescale of the star-bursting system, in this case giant molecular clouds, the luminosity grows beyond the critical luminosity and star formation rate stops. This could explain the narrow burst length observed in the cluster formation rate. Solomon et al. (1987) give typical values for molecular clouds in the Galaxy. The dynamical time scale can be estimated by: $t_{\text{dyn}} \simeq R_{\text{eff}}/\sigma = R_{\text{eff}}^{1/2}/\sigma$, where σ is the velocity dispersion inside the cloud. Thus, t_{dyn} is between 6 - 15 Myr for molecular clouds in the mass range $10^6 - 10^{7.5} M_{\odot}$ as found in M51 (Rand & Kulkarni 1990), which are the most likely progenitors of star clusters in M51. This may explain the short duration of the burst in M51.

6.3. Spatial Dependence of the Cluster Formation Rate

Figure 13 shows that the cluster formation history does not differ significantly between the two sides of the galaxy, although the west side of the galaxy seems to have approximately twice as many clusters as the east side. This is not an effect of the differing detection limits between the two pointings, as we have restricted our analysis to magnitudes brighter than the 90% completeness limit of the shallowest observation.

The higher cluster formation rate on the west side of the galaxy is also reflected in the presence of large, isolated and young star cluster complexes located in the western spiral arms, that appear to be largely absent in the eastern spiral arms (Bastian & Gieles 2004). These complexes are typically less than ~ 6 Myr old, contain 3×10^4 to $3 \times 10^5 M_{\odot}$, and are associated with large concentrations of CO (Henry et al. 2003).

Henry et al. (2003) studied the present day star formation rate (SFR) and its relation to the molecular cloud content in the spiral arms of M51, based on NICMOS (Pa α) and BIMA-SONG (CO 1-0) observations. They find that both the molecular cloud content and the SFR are higher in the NW and W spiral arm (regions 1a and 1b in their terminology) than in the SE and E arm (regions 2a and 2b). Thus the larger amount of clusters that we find in the western arm is consistent with the measured higher SFR on this side of the galaxy.

7. A population of short-lived clusters

As noted in § 6.2, the cluster formation history of M51 shows a large increase during that last ~ 6 Myr (see Fig. 12). This can be interpreted in two ways, either M51 is experiencing a burst in cluster formation right now, or that a significant portion of the very young clusters (< 10 Myr old) will disrupt within the next few Myr. Three additional observations argue for the latter scenario. First, a similar feature has been observed in the NGC 4038/39 system (Whitmore 2003). Second, we know of many loose open star clusters within the Galaxy that are expected to disperse on timescales shorter than 10 Myr (e.g. Lada & Lada 1991). Lastly, ~ 10 Myr is the timescale given

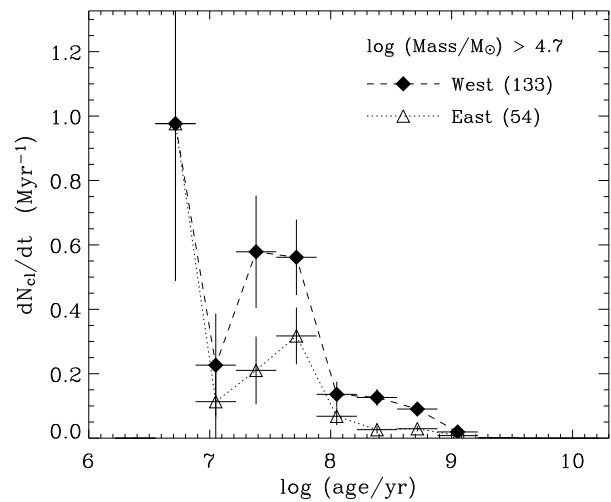


Fig. 13. Spatial dependence of the cluster formation rate. We have not corrected the rates here for fitting errors. We note that the general trend in the formation rate is similar between the two sides of the galaxy.

for NGC 5253 for clusters to dissolve and disperse their stars into the field (Tremonti et al. 2001). Adopting this scenario, we can explore what percentage of the young clusters will disrupt within the next few Myr.

To do this we compare the observed “formation” rates in the first two bins of Fig. 12, i.e. the bins of $\log(t/\text{yr})=6.6$ to 6.93 , and 6.93 to 7.26 . In Fig. 14 we show the percentage of the young clusters that are expected to disrupt before they age to older than 10 Myr, as a function of their mass. One striking feature of this figure, is that the percentage of the clusters disrupted is largely independent of mass within the uncertainties of the measurements.

The mean value of the number ratio of clusters in the logarithmic age bins of $(6.93, 7.26)$ compared to $(6.6, 6.93)$ for clusters with a mass in the range of $3.5 < \log(M/M_{\odot}) < 5.0$ is $68 \pm 15\%$. This is comparable to the fraction ($\sim 87\%$) of missing clusters less than 10^8 years (observed relative to predictions based on embedded star clusters in GMCs) in the solar neighbourhood estimated by Lada & Lada (1991). This missing fraction is presumably made up of unbound clusters that have dispersed. For clusters to disappear from our sample due to expansion, their radius should extend over more than ~ 3 pixels (with the exact value depending on the cluster’s brightness and the brightness of the local background), corresponding to a linear size of 48 pc. For a mean initial velocity dispersion of the stars in a cluster of about 10 km s^{-1} , this corresponds to a disruption time of about 5 Myr.

The largely mass independent destruction rate of the clusters is in stark contrast to other observed disruption patterns (Boutloukos & Lamers 2003) in which the disruption timescale is heavily dependent on the initial mass of the cluster. Boutloukos & Lamers (2003) found that the

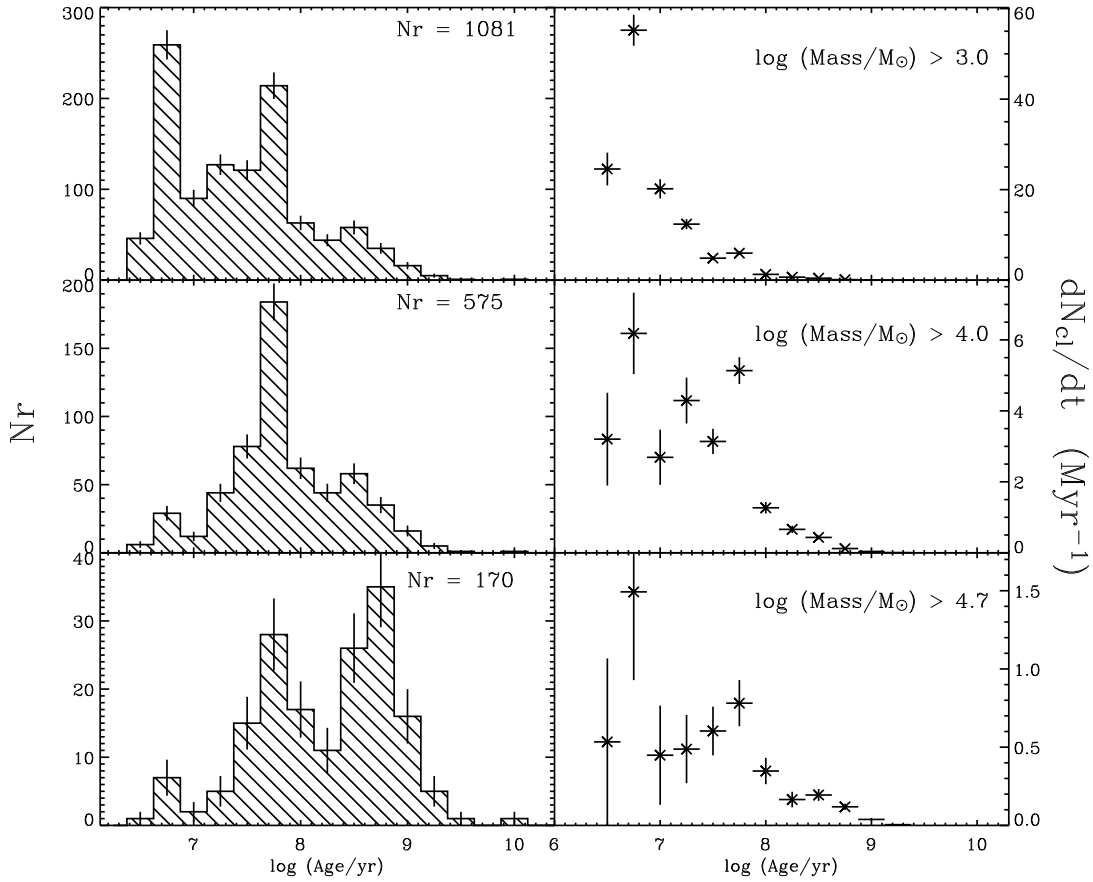


Fig. 12. Differences between the age distribution and the formation distribution. Left: the number of clusters found per age bin for three mass limits. Right: the cluster formation rate (number per Myr) as a function of age, corrected for the recovery errors given in Fig. 7. Adopting different mass limits clearly biases the interpretation of the distribution.

disruption time depends on the cluster mass to the power 0.6 for cluster systems in four different galaxies. Also theoretical disruption studies of young cluster populations (e.g. Vesperini 1998, Fall & Zhang 2001, Baumgardt & Makino 2003) have shown a strong dependence of the disruption timescale on the mass of the cluster. This implies that there are two distinct stages of disruption. The first, mass independent, operates on very short timescales and may be related to the sudden removal of gas from the system caused by supernovae and stellar winds (Boily & Kroupa 2003). This effect has been dubbed “infant mortality” (e.g. Whitmore 2004) and it corresponds to the rapid disruption of unbound clusters. The second stage of disruption, strongly mass dependent, operates on longer timescales and is a combination of different effects, including evaporation, tidal fields, and relaxation.

Indeed, we expect that the first period of disruption is largely mass independent in order that the mass functions (as interpreted through the luminosity function) of extremely young (< 10 Myr) cluster systems such as in the Antennae (Whitmore et al. 1999) is similar to that of intermediate-age populations (300 Myr - 3 Gyr) such as in

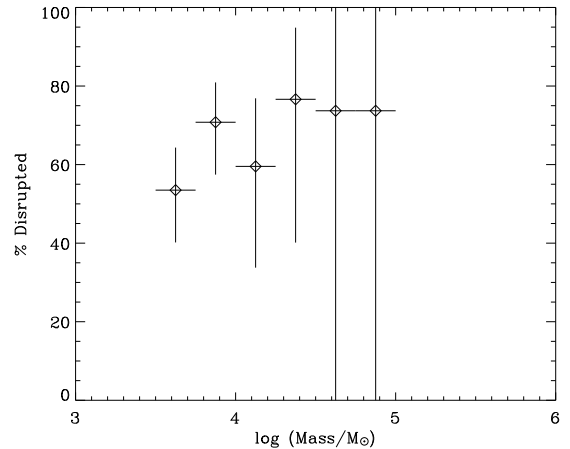


Fig. 14. The fraction of the young (< 10 Myr old) clusters per mass bin that are expected to be disrupted within the next ~ 10 Myr.

NGC 7252 (Miller et al. 1997) and NGC 3610 (Whitmore et al. 2002).

8. Cluster sizes

Using the `ishape` algorithm by Larsen (1999), we have attempted to derive the effective radius of all clusters on the WF chips in M51 with an observed F439W magnitude brighter than 22.6 mag. We have restricted ourselves to these brighter clusters, as fainter clusters do not have a high enough signal-to-noise ratio for unambiguous model fits. Briefly, the algorithm convolves a two dimensional analytical model (e.g. a King profile) with the PSF and diffusion kernel of the F555W filter for a given WFPC2 chip. We have modelled the PSF of the F555W filter with *Tiny Tim*, at position $x = 400, y = 400$ for each of the three wide field chips. We have tested whether the fits change significantly if the PSF used is from a different portion of the chip, and find that the difference is marginal, on the order of 10% in the derived radius. The algorithm then compares the model with the observed cluster profile using a reduced χ^2 test. For each observed cluster, multiple King profiles, all with concentration factor 30, of varying sizes were compared and the best fit model was selected. We then converted the measured FWHM of the profile to effective radius, R_{eff} (Larsen 1999).

Following Larsen (2004), the minimum value accepted for a 'resolved' cluster was a FWHM of 0.2 pixels. At the distance of M51, a FWHM of 0.2 pixels for a King profile with concentration factor 30 corresponds to an R_{eff} of 1.2 pc. We adopt the more conservative lower limit of 2 pc when making the subsample of resolved clusters from the full cluster sample. We caution that this size criterion biases the sample towards large clusters, but due to the resolution of the data, clusters smaller than this criterion do not have well determined radii. This results in 407 clusters that pass the criteria given in § 4.4, have reliable size measurements of ≥ 2 pc and are located more than 3 pixels away from the nearest source. The final criterion was applied in order to avoid contamination by neighboring sources in the size determination. The size criterion ($R_{\text{eff}} \geq 2$ pc) eliminates 552 clusters from the sample. Of the 91 sources that were detected in four or more bands, did not pass our $\sigma^2(BVR)$ criterion, and were brighter than $V = 22.0$, 84% were unresolved. This provides further evidence that our cluster selection eliminates the majority of contaminating individual stars from our sample.

Additionally, we have tested the reliability of the derived fit as a function of the magnitude of the cluster. To do this we generated 20 artificial clusters with effective radii between 0.65 and 12.4 pc for magnitudes $V = 20, 21, 22$, and 23 mag (i.e., 80 clusters in total). We added these analytic profiles to the F555W images and re-fit them using the above method. Figure 15 shows the results of these tests. As a function of decreasing brightness, the first clusters to deviate from the input radius are the large clusters. This is due to the fact that the outer parts of the clusters will be lost in the background noise, and so larger clusters will be affected first.

The distribution of sizes for all clusters more than 3 pixels away from the nearest source, is shown in Fig. 16.

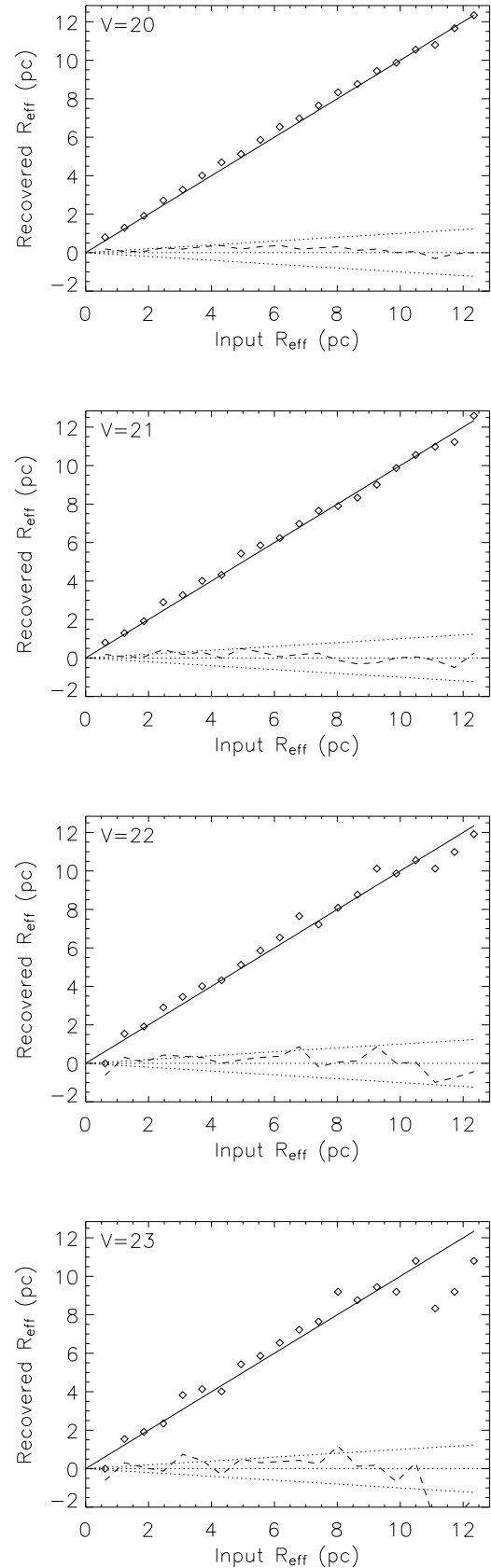


Fig. 15. A test of the accuracy of the measurements of cluster radii. The derived effective radius as a function of both the input effective radius and the magnitude. A one-to-one relation is shown by the solid line. The difference between the recovered and the input radii is shown as the dashed line, while the dotted lines show the value 10% difference between the input and the recovered radii.

The dashed line in the figure is a power-law fit to the data of the form $N(r)dr \propto r^{-\eta}dr$, with $\eta = 2.2 \pm 0.2$, where the fit was carried out only on clusters with $R_{\text{eff}} > 2$ pc (i.e. the resolved sample) and $R_{\text{eff}} < 15$ pc (most larger sources were determined to be blends of sources upon visual inspection). We note that this fit overestimates the number of small clusters, a possible indication of a turnover in this distribution. We compare this to the size distribution of the Galactic globular clusters, by using the data available in the McMaster catalog (Harris 1996)⁴. Fig. 17 shows the size distribution (half-mass radius) of the Galactic globular clusters, along with the best fitting power-law with $\eta = 2.4 \pm 0.5$. We note that the size distribution of the M51 clusters is different from that reported for the young cluster system in the merger remnant NGC 3256, which is characterized by $\eta = 3.4$ (Ashman & Zepf 2001). In that same work, the authors report that the size distribution of the Galactic globular clusters has $\eta = 3.4$, significantly steeper than that found here (although using the same catalog). This may have been caused by the erroneous addition of +1 to η in the fitting of the size distribution (see Elmegreen & Falgarone 1996 for a correction of a similar point of confusion in the data of Galactic GMCs). We therefore report that the size distribution of the old Globular clusters in the Galaxy and that of the young M51 clusters (and possibly that of the young NGC 3256 system) has the same form, within the errors. This distribution is, however, significantly different from the Galactic GMC size distribution, which is characterized by $\eta = 3.3 \pm 0.3$ (Elmegreen & Falgarone 1996), in contrast with what was reported by Ashman & Zepf (2001).

The similarity between the size distributions of MW GCs and young star clusters suggests that disruption processes (which have had a much longer time to act on the MW GCs) have not preferentially acted upon the larger clusters. Thus, cluster disruption appears to be largely independent of size. Additionally, the strong resemblance between size distributions of M51 and the Galactic globular clusters lends support to the idea of a universal formation mechanism for star clusters.

9. Correlations with the cluster radius

With a dataset such as compiled in this work, it is interesting to search for correlations among the derived parameters. In particular we are interested in relations which may reflect the formation mechanism of star clusters. Much emphasis has been placed on the relation between the size of a cluster and the cluster's mass/luminosity (e.g. Zepf et al. 1999, Ashman & Zepf 2001). The GMCs that are presumed to be the birth place of young clusters follow the relation $r_{\text{cloud}} \propto M_{\text{cloud}}^{1/2}$ (Larson 1981). Young clusters, such as those in merging galaxies (Zepf et al. 1999) and in spiral galaxies (Larsen 2004) show only a slight correlation (if at all) between their radii and masses. The results

⁴ We used the revised February 2003 version, <http://physun.physics.mcmaster.ca/Globular.html>

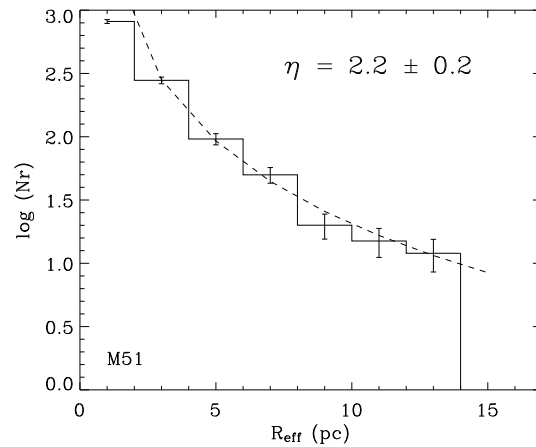


Fig. 16. Size distribution of all clusters more than 3 pixels away from the nearest source. The dashed line is a power-law fit to the data of the form $N(r)dr \propto r^{-\eta}dr$, with $\eta = 2.2 \pm 0.2$. The fit was carried out for all clusters with $2.0 < R_{\text{eff}} < 15.0$ pc. The power-law fits the data quite well for sources greater than 2 pc, although it over-estimates the number of small clusters (unresolved clusters were given a size of 0 pc) with respect to the observations.

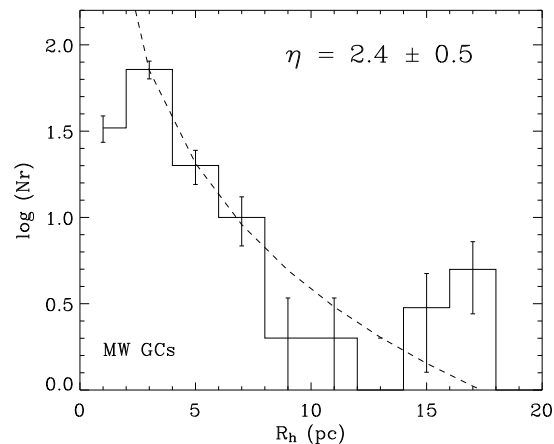


Fig. 17. Size distribution (half mass radius) of the Galactic globular cluster population. The dashed line is a power-law fit to the data of the form $N(r)dr \propto r^{-\eta}dr$, with $\eta = 2.4 \pm 0.5$. The fit was carried out for all clusters with $2.0 < R_{\text{eff}} < 15.0$ pc.

using our sample are shown in Fig. 18. There is no apparent direct relation between the mass and size of a cluster in M51.

Recently, Larsen (2004) has shown that young clusters in spiral galaxies have shallower luminosity profiles than older clusters, presumably due to an extended halo surrounding young clusters, although no correlation between size and age is found. In § 8 we presented our method used to derive the cluster sizes, which assumed a constant cluster profile, unlike the study of Larsen (2004) which

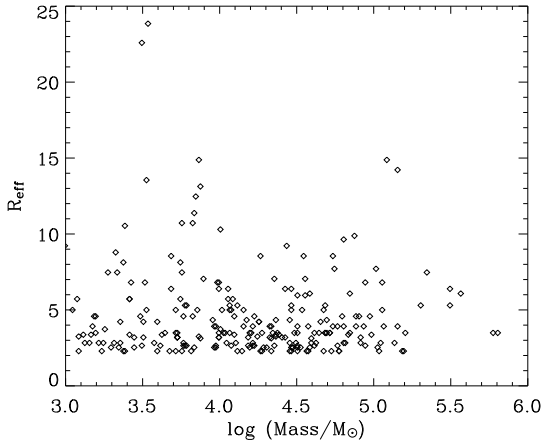


Fig. 18. The cluster mass vs. radius for all clusters with $R_{\text{eff}} > 2$ pc and located more than 3 pixels away from the nearest neighboring source.

also solved for the best fitting cluster profile. Figure 19 shows the effective radii vs. ages for the resolved clusters in our M51 sample. No strong correlation is found, although there is a slight tendency for younger clusters to be more extended than their older counterparts. We also note that if we include the unresolved clusters (assigning an effective radius of 1 pc) this slight trend is removed.

We have also attempted a multi-variable fit of the form:

$$R_{\text{eff}} = b \times \text{age}^x * \text{mass}^y. \quad (2)$$

The derived exponents, x and y , are -0.051 ± 0.027 and 0.048 ± 0.031 , respectively, if we restrict the sample to only the most robust measurements, $3 < R_{\text{eff}}(\text{pc}) < 10$ and sources more than 5 pixels away from the nearest source. As before we see a slight trend of the size decreasing with increasing age as well as a slight increase in size with increasing mass, though both relations are quite shallow and have rather large uncertainties.

Van den Bergh et al. (1991) report that globular clusters in the Galaxy follow the relation $D_{\text{eff}} \propto R_{\text{gal}}^{1/2}$ (with a large scatter) where D_{eff} is the diameter within which half the light of the cluster is contained, in projection, and R_{gal} is the distance of the cluster to the Galactic center. They interpret this result as suggesting that compact clusters form preferentially near the centers of galaxies where the density of gas clouds is higher than in the outer regions of the galaxy. We have searched our sample in two ways to see if a similar effect is present. We have looked for a relation between the effective radius of a cluster and its galactocentric distance (Fig. 20) as well as a trend between the stellar density (instead the effective radius) of each cluster and its galactocentric distance (Fig. 21). No clear relation can be seen. This may mean that the young clusters are forming by a different mechanism than globular clusters. This may simply be due to our sample coming mainly from the disk of M51 while the globular clusters presum-

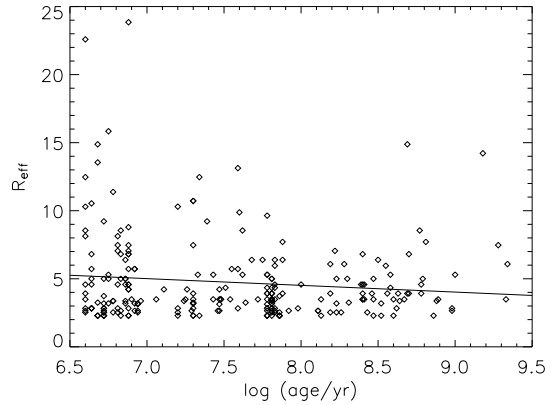


Fig. 19. The age of the clusters vs. their effective radii. There is a slight tendency for younger clusters to be larger than their older counterparts, but the scatter is large.

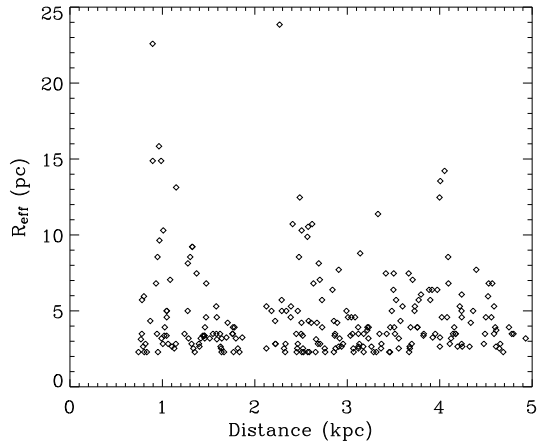


Fig. 20. The effective radii of a clusters versus their distance to the nucleus of M51. No trend is apparent in the data.

ably formed outside the Galactic disk. Alternatively, the relation found for old globular clusters in the Galaxy may be due to disruption effects which have had a much longer time to work on globular clusters than on the young disk population in the M51 sample.

10. Conclusions

We have analysed the star cluster population of the interacting galaxy M51. By comparing the broad-band magnitudes with those of SSP models, we have derived the ages, extinction values and masses of 1152 clusters with ages between 4 Myr and 10 Gyr, and masses between $10^{2.7} - 10^6 M_{\odot}$. The main conclusions can be summarized as follows:

1. In order to examine the cluster formation history within a galaxy, a minimum mass cut-off must be applied, above which the sample is complete over the

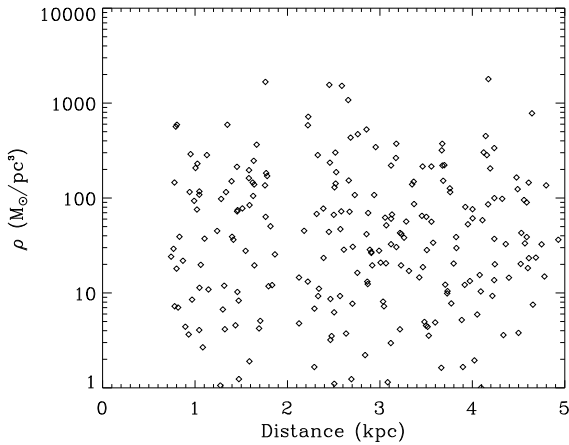


Fig. 21. The density of the clusters versus their distance to the nucleus of M51. No trend is apparent in the data.

entire age range of interest. This avoids the bias introduced by the effects of the fading of clusters due to stellar evolution.

2. The cluster formation rate increased significantly approximately 60 Myr ago, which is coeval with the proposed *second encounter* between M51 and its companion NGC 5195. We interpret this as evidence supporting the multiple encounter model of Salo & Laurikainen (2000).
3. The number of young (< 10 Myr) clusters is much higher than would be expected for a constant cluster formation rate over the past 20-30 Myr. By comparing the formation rate during the past 10 Myr to that between 10-20 Myr, we find that $\sim 70\%$ of the young clusters will disrupt before they are 10 Myr old. This process appears to be independent of mass, which implies that it is a fundamentally different disruption mechanism from that which dominates the disruption of older clusters. Thus, there seem to be at least *two* distinct modes of cluster disruption. The first mechanism operates during the first ~ 10 Myr of the cluster's lifetime while the second operates on significantly longer timescales. We suggest that the first may be due to rapid gas removal from the emerging young cluster, based on the models of Boily & Kroupa (2003). This is similar to the fraction of unbound clusters in the solar neighbourhood. The second mechanism has been extensively modelled (e.g. Vesperini 1998, Fall & Zhang 2001, Baumgardt & Makino 2003) and includes two-body encounters within the cluster, disk shocking, and stellar evolutionary processes. This disruption mechanism was studied for M51 by Boutloukos and Lamers (2003), based on the cluster study in one of the WFPC2 chips presented in Paper I. We will improve this disruption study in detail in Paper III, based on the new and largely extended cluster sample presented in this paper.

4. The western side of M51 contains a significantly higher number of star clusters, although the age and mass distributions of the clusters present do not show any large discrepancies. This trend is also reflected in the presence of large, isolated, and young star cluster complexes located in the west spiral arm, which appear to be absent on the east side of the galaxy. This is also consistent with the estimated star formation rates of Henry et al. (2003).
5. The cluster effective radius distribution can be well approximated by a power-law of the form $N(r)dr \propto r^{-\eta}dr$, with $\eta = 2.2 \pm 0.2$. This is remarkably similar to the distribution of old Milky Way Globular Clusters, which is characterized by $\eta \simeq 2.4 \pm 0.5$. These distributions are significantly different from the Galactic giant molecular cloud (GMC) distribution ($\eta = 3.3$). The agreement between the size distributions of the old Galactic globular clusters and the young clusters in M51 suggests that cluster disruption is largely independent of cluster size and argues for a universal cluster formation mechanism.
6. We have searched our dataset in order to look for correlations among the derived parameters. From this study we report that:
 - (a) We find a strong correlation between the age of a cluster and its extinction, with the youngest clusters (< 10 Myr) having $< A_V > \approx 0.55$ mag, while the oldest clusters (~ 1 Gyr) have $< A_V > \approx 0.30$ mag. At an age of ~ 20 Myr the extinction drops suddenly, and then remains relatively constant for older ages. This is qualitatively expected as clusters emerge from the molecular cloud from which they formed.
 - (b) A shallow relation is found between the effective radius of a cluster and its mass.
 - (c) There is a marginal correlation between the age of a cluster and its effective radius, with young clusters being slightly larger than older ones.
 - (d) Contrary to observations of globular clusters in the Galaxy, no correlation between the size of a cluster and its galactocentric radius is found. Additionally, no correlation between density and galactocentric radius is apparent in our dataset.

Acknowledgements. We thank Søren Larsen for useful discussions of the work and comments on the draft, both before and during the refereeing process. Additionally, we thank Michael Fall, Brad Whitmore, and Rupali Chandar for useful discussions, and Phillip Massey for help in estimating the contamination by field stars. We also thank Cees Bassa for making Figs. 1 & 2.

References

- Anders, P., & Fritze-v. Alvensleben., U. 2003, A&A, 401, 1063
 Anders, P., Bissantz, N., Fritze-v. Alvensleben, U., & de Grijs, R. 2004, MNRAS, 347, 196
 Ashman, K.M., & Zepf, S.E. 2001, AJ, 122, 1888

- Bastian, N., & Lamers, H.J.G.L.M. 2003, in *Extragalactic Globular Cluster Systems*, ed. M. Kissler-Patig *ESO Astrophysics Symposia* (Springer: Berlin), 28
- Bastian, N., & Gieles, M. 2004, in *The Formation and Evolution of Massive Young Star Clusters*, eds. H.J.G.L.M. Lamers, A. Nota, & L.J. Smith, *ASP Conf. Ser.* (in press)
- Baumgardt H., & Makino J. 2003, *MNRAS*, 340, 227
- Bessell, M.S., Castelli, F., & Plez, B. 1998, *A&A*, 33, 231
- Bica, E., Clariá, J.J., Dottori, H., Santos, J.F.C. Jr., & Piatti, A.E. 1996, *ApJSS*, 102, 57
- Bik, A., Lamers, H.J.G.L.M., Bastian, N., Panagia, N., & Romaniello, M. 2003, *A&A*, 397, 473 (Paper I)
- Boily, C.M & Kroupa, P., 2003, *MNRAS*, 338, 665
- Boutloukos, S.G. & Lamers, H.J.G.L.M. 2003, *MNRAS*, 338, 717
- de Grijs, R., Bastian, N., & Lamers, H.J.G.L.M. 2003a, *MNRAS*, 340, 197
- de Grijs, R., Fritze-v. Alvensleben, U., Anders, P., Gallagher, J.S., Bastian, N., Taylor, V.A., & Windhorst, R.A. 2003b, *MNRAS*, 342, 259
- de Grijs, R., Anders, P., Bastian, N., Lynds, R., Lamers, H.J.G.L.M., & O’Neil, E.J. 2003c, *MNRAS*, 343, 1285
- Dolphin, A.E., Kennicutt, R.C., Jr. 2002, *AJ*, 124, 158
- Elmegreen, B.G., 1996, *ApJ*, 471, 816
- Fall, S.M. & Zhang, Q. 2001, *ApJ* 561, 751
- Feldmeier, J.J., Ciardullo, R., & Jacoby, G.H. 1997, *ApJ*, 479, 231
- Gieles, M., Bastian, N., & Lamers, H.J.G.L.M. 2004, Paper III (in prep).
- Grimm, H.-J., Gilfanov, M., Sunyaev, R. *MNRAS*, 2003, 339, 793
- Harris, W.E. 1996, *AJ*, 112, 1487
- Harris, W.E., & Pudritz, R.E. 1994, *ApJ*, 429, 177
- Henry, A.L., Quillen, A.C., & Gutermuth, R. 2003, *AJ*, 126, 2831
- Hernquist, L. 1990, in Wielen R., ed., *Dynamics and Interactions of Galaxies*. Springer, Heidelberg, p.108
- Hill, J.K., Waller, W.H., Cornett, R.H., et al. 1997, *ApJ*, 477, 673
- Holtzman, J.A., Hester, J.J., Casertano, S., et al. *PASP*, 107, 156
- Humphreys, R.M., & Davidson, K. 1979, *ApJ*, 232, 409
- Krist, J., & Hook, R. 1997, “The Tiny Tim User’s Guide”, *STScI*
- Lada, C.J., & Lada E.A. 1991, in *The formation and evolution of star clusters*, ed. K. Joes, *ASP Conf. Ser.*, Vol. 13 p. 3
- Lançon, A., & Mouhcine, M. 2000, in *Massive Stellar Clusters*, eds. A. Lançon & C. Boily, *Astronomical Society of the Pacific Conference Series*, p. 34
- Larsen, S.S. 1999, *A&AS*, 139, 393
- Larsen, S.S. 2000, *MNRAS*, 319, 893
- Larsen, S.S. 2002, *AJ*, 124, 1393
- Larsen, S.S. 2004, *A&A*, 416, 537
- Larson, R.B. 1981, *MNRAS*, 194, 809
- Leitherer, C., Schaerer, D., Goldader, J. D., et al. 1999, *ApJS*, 123, 3
- Massey, P., Lang, C.C., DeGioia-Eastwood, K., & Garmany, C.D. 1995, *ApJ*, 438, 188
- Massey, P. 2002, *ApJS*, 141, 81
- Meatheringham, S.J. 1991 in *The Magellanic Clouds*, eds. R. Haynes & D. Milne (Kluwer, Dordrecht), 89
- Miller, B.W., Whitmore, B.C., Schweizer, F., & Fall, S. M. 1997, *AJ*, 114, 2381
- Murray, N., Quataert, E., Thompson, T.A. 2004, *ApJ* (submitted: astro-ph/0406070)
- Parmentier G., de Grijs R., & Gilmore G.F., 2003, *MNRAS*, 342, 208
- Rand, R.J. & Kulkarni, S.R. 1990, *ApJ*, 349, L43
- Romaniello, M, Panagia, N., Scuderi, S., & Kirshner, R.P. 2002, *AJ*, 123, 915
- Salo, H., & Laurikainen, E. 2000, *MNRAS*, 319, 377
- Savage, B.D., & Mathis, J.S. 1979, *ARAA*, 17, 73
- Schulz, J., Fritze-v. Alvensleben, U., & Fricke, K.J. 2002, *A&A*, 392, 1
- Scoville, N.Z., Polletta, M., Ewald, S., Stolovy, S.R., Thompson, R., & Rieke, M. 2001, *AJ*, 122, 3017
- Solomon, P.M., Rivolo, A.R., Barrett, J., & Yahil, A. 1987, *ApJ*, 319, 730
- Stetson, P.B. 1987, *PASP*, 99, 191
- Tremonti, C.A., Calzetti, D., Leitherer, C., & Heckman, T.M. 2001, *ApJ*, 555, 322
- Toomre, A., & Toomre, J., 1972, *ApJ*, 319, 623
- Vesperini, E. 1998, *MNRAS*, 299, 1019
- van den Bergh, S., & Morbey, C. 1991, *ApJ*, 375, 594
- van Dokkum, P.G. 2001, *PASP*, 113, 1420
- Voit, M., 1997, *HST Data Handbook*, STScI
- Westerlund, B. E. 1997, *The Magellanic Clouds* (Cambridge: Cambridge Univ. Press)
- Whitmore, B.C., Heyer, I., & Casertano, S. 1999, *PASP*, 111, 1559
- Whitmore, B.C. Zhang, Q., Leitherer, C., et al. 1999b, *AJ*, 118, 1551
- Whitmore, B.C., Schweizer, F., Kundu, A., & Miller, B. 2002, *AJ*, 124, 147
- Whitmore, B.C. & Zhang, G. 2002, *AJ*, 124, 1418
- Whitmore, B.C. 2003, in *A Decade of HST Science*, eds. M. Livio, K. Noll, & M. Stiavelli, (Cambridge: Cambridge University Press), 153
- Whitmore, B.C. 2004, in *The Formation and Evolution of Massive Young Star Clusters*, eds. H.J.G.L.M. Lamers, A. Nota, & L.J. Smith, *ASP Conf. Ser.* (in press)
- Zepf, S.E., Ashman, K.M., English, J., Freeman, K.C., Sharples, R.M. 1999, *AJ*, 118, 752